DOT/FAA/RD-93/14

Project Report
ATC-199

Contributions to the American Meteorological Society's 26th International Conference on Radar Meteorology

M. M. Wolfson

1 April 1993

Lincoln Laboratory
MASSACHUSETTS INSTITUTE OF TECHNOLOGY
LEXINGTON, MASSACHUSETTS

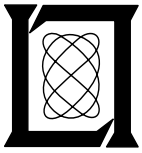

Prepared for the Federal Aviation Administration,
Washington, D.C. 20591

TECHNICAL REPORT STANDARD TITLE PAGE

1. Report No.	2. Government Accession No.	3. Recipient's Catalog No.
ATC-199	DOT/FAA/RD-93/14	

4. Title and Subtitle	5. Report Date
Contributions to the American Meteorological Society's 26th International Conference on Radar Meteorology	1 April 1993
	6. Performing Organization Code

7. Author(s)	8. Performing Organization Report No.
Marilyn M. Wolfson, Editor	ATC-199

9. Performing Organization Name and Address	10. Work Unit No. (TRAIS)
Lincoln Laboratory, MIT P.O. Box 73 Lexington, MA 02173-9108	11. Contract or Grant No. DTFA-01-91-Z-02036

12. Sponsoring Agency Name and Address	13. Type of Report and Period Covered
Department of Transportation Federal Aviation Administration Systems Research and Development Service Washington, DC 20591	Project Report
	14. Sponsoring Agency Code

15. Supplementary Notes

This report is based on studies performed at Lincoln Laboratory, a center for research operated by Massachusetts Institute of Technology under Air Force Contract F19628-90-C-0002.

16. Abstract

Eleven papers contributed by the Lincoln Laboratory Weather Sensing Group to the American Meteorological Society's 26th International Conference on Radar Meteorology, to be held May 24-28, 1993 in Norman, Oklahoma, are compiled in this volume. The work reported was sponsored by several FAA programs, including Terminal Doppler Weather Radar (TDWR), Air Surveillance Radar-9 (ASR-9), Integrated Terminal Weather System (ITWS), and Terminal Area Surveillance System (TASS). The papers are based on analyses completed over the past year at Lincoln Laboratory and in collaboration with staff at the National Severe Storms Laboratory, the University of Oklahoma, Raytheon Corporation, and the FAA Technical Center in Atlantic City, NJ.

The staff members of the Weather Sensing Group have documented their studies in four major areas: Operational Systems (TDWR Operational Test and Evaluation results); Radar Operations (future airport weather surveillance requirements, a "machine intelligent" gust front detection algorithm, microburst asymmetry study results, a shear-based microburst detection algorithm, and a hazard index for TDWR-detected microbursts); Signal Processing (coherent processing across multi-PRI waveforms, clutter filter design for multiple-PRT signals, and identification of anomalous propagation associated with thunderstorm outflows); and Analysis Methods (multiple-single Doppler wind analysis using NEXRAD data, and an adjoint method wind retrieval scheme).

17. Key Words	18. Distribution Statement
microburst asymmetry microburst detection gust front detection Terminal Doppler Weather Radar (TDWR) Air Surveillance Radar-9 (ASR-9) windshear hazard index clutter filter design multiple Doppler analysis Integrated Terminal Weather System (ITWS) multi-PRI waveforms anomalous propagation adjoint methods Terminal Area Surveillance System (TASS)	This document is available to the public through the National Technical Information Service, Springfield, VA 22161.

19. Security Classif. (of this report)	20. Security Classif. (of this page)	21. No. of Pages	22. Price
Unclassified	Unclassified	46	

FORM DOT F 1700.7 (8-72) Reproduction of completed page authorized

ABSTRACT

Eleven papers contributed by the Lincoln Laboratory Weather Sensing Group to the American Meteorological Society's 26th International Conference on Radar Meteorology, to be held May 24–28, 1993 in Norman, Oklahoma, are compiled in this volume. The work reported was sponsored by several FAA programs, including Terminal Doppler Weather Radar (TDWR), Air Surveillance Radar–9 (ASR–9), Integrated Terminal Weather System (ITWS), and Terminal Area Surveillance System (TASS). The papers are based on analyses completed over the past year at Lincoln Laboratory and in collaboration with staff at the National Severe Storms Laboratory, the University of Oklahoma, Raytheon Corporation, and the FAA Technical Center in Atlantic City, NJ.

The staff members of the Weather Sensing Group have documented their studies in four major areas: **Operational Systems** (TDWR Operational Test and Evaluation results); **Radar Operations** (future airport weather surveillance requirements, a "machine intelligent" gust front detection algorithm, microburst asymmetry study results, a shear–based microburst detection algorithm, and a hazard index for TDWR–detected microbursts); **Signal Processing** (coherent processing across multi–PRI waveforms, clutter filter design for multiple–PRT signals, and identification of anomalous propagation associated with thunderstorm outflows); and **Analysis Methods** (multiple–single Doppler wind analysis using NEXRAD data, and an adjoint method wind retrieval scheme).

CONTENTS

PRELIMINARY RESULTS OF THE WEATHER TESTING COMPONENT OF THE TERMINAL DOPPLER WEATHER RADAR OPERATIONAL TEST AND EVALUATION

Steven V. Vasiloff[1], Michael D. Eilts[1], Elizabeth Turcich[2],
Jim Wieler[3], Mark Isaminger[4], and Paul Biron[4]

[1]National Severe Storms Laboratory
Norman, Oklahoma 73069

[2]Federal Aviation Administration Technical Center
Atlantic City International Airport
Atlantic City, New Jersey 08405

[3]Raytheon Corp.
Sudbury, Massachusetts 01776

[4]Massachusetts Institute of Technology/Lincoln Laboratory
Lexington, Massachusetts 02173

1. INTRODUCTION

The Terminal Doppler Weather Radar (TDWR) system (Turnbull et al. 1989), which has been developed by Raytheon Co. for the Federal Aviation Administration (FAA), provides automatic detection of microbursts (Fujita 1985) and low-altitude wind shear. Microburst- and gust front-induced wind shear can result in a sudden, large change in airspeed which can have a disastrous effect on aircraft performance during take off or landing. The second major function of TDWR is to improve air traffic management through forecasts of wind shifts, precipitation and other weather hazards. The TDWR system generates Doppler velocity, reflectivity, and spectrum width data. The base data are automatically dealiased and clutter is removed through filtering and mapping. Precipitation and windshear products, such as microbursts and gust fronts, are displayed as graphic products on the Geographic Situation Display (Fig. 1) which is intended for use by Air Traffic Control supervisors. Alphanumeric messages indicating the various windshear alerts and derived airspeed losses and gains are sent to a flat panel ribbon display which is used by the controllers in the control tower.

The TDWR proof-of-concept and operational feasibility have been demonstrated in a number of FAA-sponsored tests and evaluations conducted by

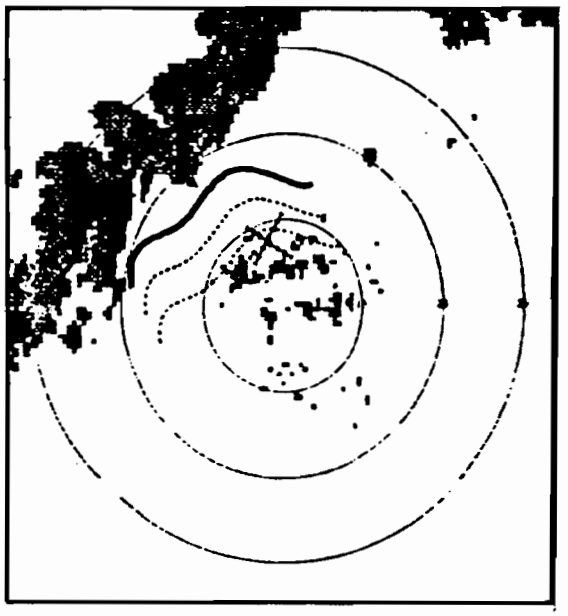

Figure 1. Black and white reproduction of a geographic situation display. The figure is centered near Wiley Post Airport. Precipitation can be seen to the west of the airport and is grey scaled (darkest is heaviest). The heavy solid line is the gust front and the dashed lines are 10 and 20-min forecasts. A control panel to the right is not shown due to space constraints. Range rings are in nautical miles.

Massachusetts Institute of Technology's Lincoln Laboratory (MIT/LL) in Memphis, TN (1985); Huntsville, AL (1986); Denver, CO (1987, 1988); Kansas City, MO (1989), and Orlando Fl. (1990-1992).

In order to verify that the TDWR meets FAA operational suitability and effectiveness requirements, an Operational Test & Evaluation (OT&E) was conducted at the Oklahoma City site during the period from 24 August to 30 October 1992. The testing addressed National Airspace System (NAS)-SS-1000 requirements, weather detection performance, safety, operational system performance, maintenance instruction books, Remote Maintenance Monitoring System (RMMS), system adaptable parameters, bullgear wear, and limited Air Traffic (AT) suitability.

The TDWR OT&E Integration and Operational testing was conducted using a variety of methods dependent on the area being tested. This paper discusses primarily the weather detection performance testing. A rough analysis was performed on the algorithm output and the base data to determine the performance of the TDWR in detecting wind shear phenomena. Final results will be available after additional testing, which is scheduled for Spring of 1993, and post analysis is conducted.

2. SYSTEM DESCRIPTION

The TDWR is a C-Band weather radar consisting of a 25-foot diameter, center-fed parabolic reflector antenna, with the feed mounted on a tripod. The antenna beamwidth is 0.55 degrees. The TDWR transmitter tube is a 250 kW peak-power pulsed klystron, transmitting a 1.1 microsecond pulse (-6 dB width) at pulse repitition frequencies from 250 to 2000 Hz. Large dynamic range is provided for both good clutter suppression and accurate reflectivity measurements. The total dynamic range, over 128 dB, is obtained with 26 dB of Sensitivity Time Control (STC), 42 dB of Automatic Gain Control (AGC), and circuits linear over 61 dB. For more detail on system characteristics the reader is referred to Wieler and Shrader 1991, and Michelson et al. 1990.

3. WEATHER TESTING RESULTS

This section describes results of the weather-detection component of the TDWR OT&E. The National Severe Storms Laboratory developed procedures to address three main components of the TDWR weather detecting capability: 1) Assess that the base data are of high quality; 2) Determine if the algorithms are functioning properly; 3) Verify that appropriate alarms are disseminated according to the system design.

3.1 Base data

In a qualitative assessment, the judgement of the Investigative Panel, a group of expert radar meteorologists from the National Center for Atmospheric Research (NCAR), MIT/Lincoln Laboratory and NSSL, is that the raw base data were of high quality. All of the NAS requirements related to measurements of base velocity, reflectivity, and spectrum width were fulfilled.

Suppression of ground clutter is important for "clean" base data and for prevention of false alarms. The TDWR uses two techniques to reduce contamination from ground clutter sources. The first involves the use of IIR (infinite impulse response) filters to suppress high reflectivity returns that have near-zero velocities. The second step is to generate a clutter residue editing map (CREM) on a clear day with no weather echoes. Experience has shown the best condition for taking clutter measurements is low clear-air reflectivities and a minimal amount of moving sources such as birds and insects.

Clutter map generation begins with an automated determination of a clear-air reflectivity (CAR) value. The CAR estimate and a maximum velocity threshold are then used to distinguish clutter residue from clear-air returns caused by birds and/or insects. It was determined that the process for building the CREMs may not be straightforward at each site. A large amount of bird activity (and possibly insects) as well as evolving boundary layer characteristics resulted in having to make the CAR estimate before sunrise. It is anticipated that each site will have its own peculiarities.

3.2 Algorithm performance

3.2.1 Microburst detection algorithm

The Microburst Detection Algorithm (MDA) detects low-altitude divergent shears associated with storms (Merritt et al. 1989). Since most of the data were collected in high-wind environments, classic microburst signatures were rarely seen.

Because a limited amount of data are available for evaluation, only rough assessments of the MDA performance are available. Detection performance was excellent although a number of false alarms were observed. Large flocks of birds departing from roosting sites in the early morning hours caused

divergent signatures similar to microbursts. There were numerous false alarms from this phenomena prior to the implementation of the storm cell test which validates alarms based on reflectivity aloft (Evans 1990). Many of the other false alarms were the result of clutter breakthrough or noise in the velocity data. Note the clutter breakthrough around the airport in Fig. 1.

3.2.2 Gust front detection algorithm

The Gust Front Detection Algorithm (GFDA) detects lines of convergence in Doppler radial velocity fields and forecasts the movement of these wind shifts and the winds behind them up to 20 minutes in advance (Hermes et al. 1992). An example of a gust front detection is shown in Fig. 1. Test results indicate that the forecasting function of the algorithm performed well, as did the estimation of winds behind the wind shift. As a gust front passed over Wiley Post Airport on 10 September, data from the local automatic surface observing site agreed well with the windshift value behind the gust front detection.

The GFDA performed well during the OT&E. However, as with the MDA, false alarms were observed. The majority of the false alarms were detected outside 20 km and thus would not impact the airport. Many of the GFDA false alarms were the result of vertical wind shear where the winds veered (turned) with height and were not the typical low-level jet situations which have been noted as a potential cause of false alarms. However, some false alarms were caused by more classical low-level jets. We are classifying these vertical wind shears and low-level jets as false alarms since they were not generated by a thunderstorm outflow. It could be argued, however, that these features are operationally significant. There were also a number of false alarms due to dealiasing errors and range folding. Minor software changes are being made to reduce the number of false alarms.

4. CONCLUSIONS

The initial Operational Test & Evaluation of the Terminal Doppler Radar showed that weather detection performance was generally acceptable. A set of NAS-SS-1000 requirements was satisfied. Base data quality appears to be excellent and the two primary algorithms, microburst detection and gust front detection, are in general working well. Minor software changes are being made to improve system performance.

Issues surrounding building accurate ground clutter suppression maps became apparent and will need to be addressed at future sites. Additional testing is scheduled for Spring 1993 after which final results will be published in the 5th International Aviation Weather Conference to be held in August, 1993.

5. ACKNOWLEDGMENTS

The authors would like to thank the many radar support personnel from the FAA, Raytheon Co., and Titan Corp. for their persistence in helping gather weather data. In particular, Fritz O'Hora, Jim Graffam, Bob Seiche, Jim Westwell, and Peter Guthlein spent many a dark hour at the radar site. This work has been supported by the Federal Aviation Administration under Interagency Agreement DTFA01-90-Z-02071.

6. REFERENCES

Evans, J.E., 1990: Results of the Kansas City 1989 Terminal Doppler Weather Radar (TDWR) Operational Evaluation Testing, Project Report ATC-171, MIT Lincoln Laboratory.

Fujita, T., 1985: The downburst-microburst and macroburst. Satellite and Mesometeorology Project, Dept. of Geosciences, University of Chicago.

Hermes, L. G., A. Witt, S. D. Smith, D. Klingle-Wilson, D. Morris, G. J. Stumpf, and M. D. Eilts, 1992: Gust front detection and wind shift algorithms for the Terminal Doppler Weather Radar system, J. of Applied Meteor., In Press.

Merritt, M. W., 1988: Microburst divergence detection for Terminal Doppler Weather Radar. Preprints, 24th Conference on Radar Meteor., Tallahasse. pp. 220-223. AMS, Boston, Ma.

Michelson, M.,W.W.Shrader, and J.G. Wieler, 1990: Terminal Doppler Weather Radar, Microwave Journal, Horizon House Inc. Vol. 33 No. 2, 139-148.

Turnbull, D. H., McCarthy, J., Evans J., Zrnic, D., 1989: The FAA Terminal Doppler Weather Radar (TDWR) Program. Preprints, 3rd Intl. Conference on the Aviation Weather System, pp. 414- 419. AMS, Boston,Ma.

Wieler, J. G. and W. W. Shrader, 1991: Terminal Doppler Weather Radar system characteristics and design constraints, Preprints, 25th Conf. on Radar Meteorology, pp. J7-J10. Paris, France, AMS, Boston, Ma.

QUANTIFYING AIRPORT TERMINAL AREA WEATHER SURVEILLANCE REQUIREMENTS*

Marilyn M. Wolfson and Cynthia A. Meuse
Lincoln Laboratory, Massachusetts Institute of Technology
Lexington, Massachusetts

1. INTRODUCTION

The Federal Aviation Administration (FAA) Terminal Area Surveillance System (TASS) research, engineering, and development program was initiated in part to address future weather sensing needs in the terminal area. By the early 21st century, planned systems such as the Terminal Doppler Weather Radar (TDWR) and Airport Surveillance Radar–9 (ASR–9) will be well into their designed life cycles. Any new terminal weather surveillance system should be designed to address existing deficiencies. Key unmet weather sensing needs include detections of: true 3–dimensional winds (vs. radial component), winds in the absence of precipitation, wake vortices, total lightning, hail, icing conditions, clear air turbulence, hazardous weather cells (with adequate time and space resolution), cloud cover and cloud bases (including layers), fog, and visibility (Runway Visual Range), as well as predictions of: the atmospheric conditions mentioned above, wind shifts, microbursts, tornadoes, and snow/rainfall rates (Evans 1991a, McCarthy 1991).

In this paper, we investigate the premise that hazardous weather cells are not currently being measured with adequate time and space resolution in the terminal area. Since a new surveillance system should be based on knowledge of storm dynamics, we have performed a preliminary study of update rate (using rapid scan radar data collected in Orlando), and spatial resolution required to detect rapidly developing thunderstorms and precursors to the low altitude hazards such as microbursts that they produce. Other aspects of a future radar system such as multi–parameter techniques required to discriminate between ice and water phase precipitation, etc. are not considered.

2. APPLICATIONS FOR TERMINAL AREA CONVECTIVE WEATHER INFORMATION

Past studies have shown that weather is the primary cause of serious air traffic delay at the nation's major airports (Weber et al. 1991), and a recent study at Lincoln Laboratory has shown that this delay may even be underestimated with the current reporting system. Thunderstorms and heavy fog account for the largest fraction of weather related delay. Some of this delay can be mitigated by more accurate detection and prediction of weather impacted flight routes, allowing efficient rerouting to take place. This will provide an important economic and safety benefit in the future, as increased air traffic demands maximization of capacity at our existing airports.

The newly deployed TDWRs and ASR–9s will provide a significant increase in safety in the terminal area, but these systems were not specifically designed to reduce weather related aviation system delays. The FAA has recently initiated the Integrated Terminal Weather System (ITWS) program, being developed at Lincoln Laboratory, to provide improved aviation weather information in the terminal area by integrating data and products from the FAA and NWS sensors (Evans 1991b). A key objective of the ITWS program is to increase the effective airport acceptance rate in adverse weather by providing information to support the Terminal Air Traffic Control Automation (TATCA) program. TATCA tools increase the efficiency of individual controller tasks and provide a dynamic, overall plan for traffic management throughout the terminal control region (Andrews and Welch 1989). Thus, reliable analyses and *forecasts* of weather impacted air routes, runway availability, and clear–air winds for direct use by TATCA, traffic managers, and pilots are a major goal of the ITWS system. The design of any future terminal weather surveillance system will have to consider this close coupling of weather sensing and forecasting, and air traffic capacity and efficiency enhancement programs.

The first deployment of the ITWS system will include a Microburst Prediction product, and may also include a storm location prediction based on projection of existing storms according to correlation tracking information. These predictions are performed on existing detectable radar reflectivity regions and thus are necessarily short term. Longer term predictions of weather impacted airspace will require predictions of storms that have yet to develop, and thus will either depend heavily on heuristic rules for convective initiation (Mueller and Wilson 1993) or, perhaps more likely because of accuracy requirements, will require gridded 4–D data assimilation – numerical forecasting techniques such as those being developed at NOAA's Forecast Systems Laboratory (Sherretz 1991). This type of gridded analysis system is already being used in 3–D for an ITWS terminal winds representation (Wilson et al. 1993). With or without gridded numerical forecasting techniques, convective forecasts will be required in a full 60 km radius region around the airport at least.

3. UPDATE RATE

Of all the unmet terminal weather sensing needs, the desire to predict rapidly developing convective weather is a driving factor in the proposed required update rate for a TASS weather sensor. Keeler (1991) assigns a critical time scale of 0.5 – 1.0 min for thunderstorms, and 1.0 – 2.0 min for widespread rain. There is evidence that a 1 min update rate is required for for thunderstorm outflow detection. Study has demonstrated the need for a similar update rate for thunderstorm life cycle predictions (Carbone et al. 1985).

To investigate this, rapid scan measurements were made with the TDWR testbed radar operated by Lincoln Laboratory in Orlando, FL, where the typically very unstable environment leads to rapidly developing and decaying thunderstorms. A special TASS scan was designed to cover a complete volume in 1 min with a set of elevation angles comparable to a true TDWR hazardous–weather mode scan (see Fig. 1). The scan provides uniform coverage up to 14 km AGL for a storm at 20 km range. Suitably long rapid scan datasets on multiple microburst–producing storms were gathered on Aug. 5 , Sept. 22, and Sept. 26 1992. For the identified cells (5 total), parameters

* This work was sponsored by the Federal Aviation Administration. The views expressed are those of the authors and do not reflect the official policy or position of the U.S. Government.

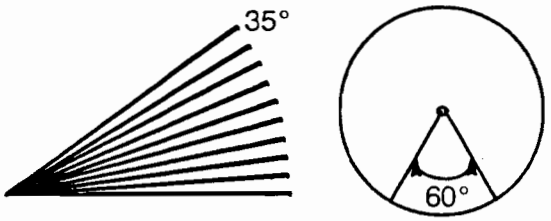

Figure 1. The TASS Rapid Volume Scan consists of 10 elevation angles (0.5, 3.7, 7.3, 10.9, 14.7, 18.6, 22.5, 26.6, 30.7, 35.0°), is 60° wide, and takes 1 min to execute with the TDWR testbed radar.

such as the average vertically integrated liquid water (VIL) and the height of the center of mass (CM) were computed. Trends in these parameters are used in the ITWS Microburst Prediction Algorithm (Wolfson et al. 1993) to identify growing thunderstorms and to predict their collapsing phase, which leads to microburst wind shear at the surface. These parameters measured every minute are compared with the identical parameters derived from hybrid TDWR volume scans made up of 3 TASS scans each, with the lowest elevation angles coming from the first TASS scan, the middle angles from the second, and the highest angles from the third. As an example, the VIL data for Aug. 5 are shown in Fig. 2a. The 3-min VIL lags and peaks later than the 1-min VIL, which shows much more detailed fluctuations. The height of center of mass data show a similar pattern (Fig. 2b).

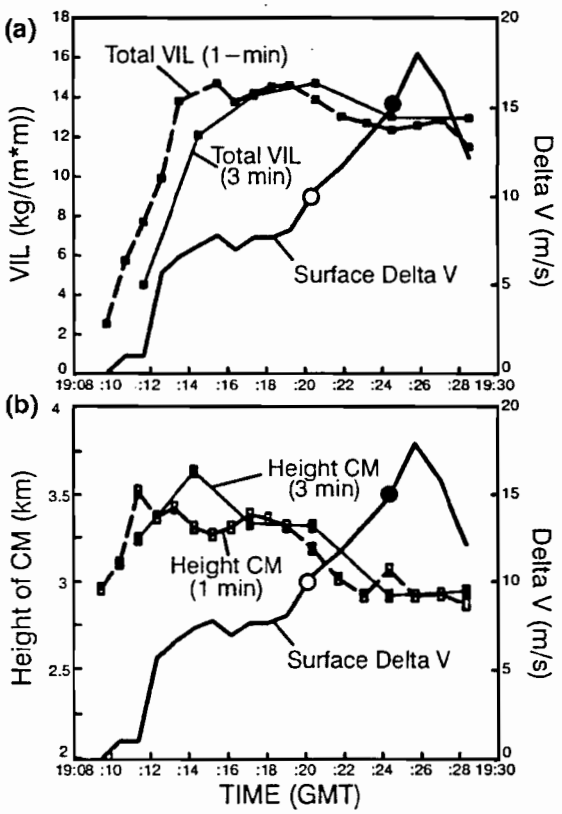

Figure 2. (a) Plot of VIL computed for a storm cell scanned with the TASS Rapid Volume Scan on August 5, 1992, and of VIL computed from 3-min hybrid scans made from the same data. The surface outflow ΔV derived from the 1-min scans is also shown. The black circle at ΔV=15 indicates the microburst onset and the white circle at ΔV=10, wind shear onset. (b) As in (a) but for height of center of mass (CM).

We used the prototype ITWS Microburst Prediction algorithm to quantify the advantage of the TASS scan (1 min) over the hybrid TDWR scan (3 min). In the algorithm, a region is first identified and tracked based on a significant rise in VIL, among other features. This rise must persist for 2 volumes for a track to be established. If the region has been tracked twice, a prediction can be issued as soon as a drop in center of mass is detected, assuming the quantity of VIL present at that time is sufficient to produce a microburst-strength outflow. Table 1 shows the achievable prediction lead times for the TASS and hybrid TDWR scans. The TASS strategy allows an average ~3 min greater prediction lead time, extending the TDWR average of 2–4 min for these (weak) cases to 5–6 min. (These results may change as the Microburst Prediction algorithm evolves from its prototypical to its final form.)

4. SPATIAL RESOLUTION

High spatial resolution is required to detect microbursts, tornadoes, etc. at very low elevation angles, but it may be possible to trade resolution for a more rapid update rate at upper levels. To investigate this, we created a model storm ellipsoid 10 km high, 6 km wide, with a central core reflectivity of 65 dBZ at 5 km AGL, which decreased linearly to the outer edges of the ellipsoid. We compared the TDWR scan to an experimental low resolution fan beam scan consisting of 6 beams, each 5° in elevation, centered at 5, 15, 25, 35, 45, and 55°. By using only 6 broad beams to scan the volume instead of 11 narrow beams (TDWR), the update rate could theoretically be improved.

Since VIL and CM measurements are crucial to the ITWS Microburst Prediction algorithm, these parameters as a function of range were compared. The ellipse was moved in range from 0 to 25 km, and "scanned" every km with both strategies. Figure 3 shows that, although the cone of silence over the radars leads to incorrect values inside of 4 km range, the values for the two strategies are not dramatically different at near range. (Even the TDWR VIL falls short of the true VIL because interpolation cannot recreate unsampled peak reflectivity regions, and the 1 km influence radius can include distant low VIL values.) At longer range, our studies have shown that the large variability of the fan beam VIL is due to the gaps in elevation, and the large rise in fan beam CM is due to the rising center height of the 15° beam, which dominates the CM calculation. For microburst prediction, the apparent changes in CM with range have far greater potential for causing false alarms than do the changes in VIL.

Since future algorithms and especially any numerical forecasting techniques will undoubtedly use gridded radar data, we also investigated the effect of Cartesian grid resolu-

Table 1. Microburst prediction lead times for 5 cells scanned with TASS scan and hybrid TDWR scan. For cases with 2 entries, first is lead time for onset of 10 m/s outflow, second for 15 m/s.

Date 1992	TDWR lead (min)	TASS lead (min)	Outflow DV (m/s)
August 5	3 – 6	6 – 9	17.5
September 22A	5	7	11.6
September 22B	3	5	14.8
September 22C	0 – 1	2 – 3	19.3
September 26	0	6	12.0
Average 10 m/s:	2.2	5.2	5 cases
Average 15 m/s:	3.5	6.0	2 cases

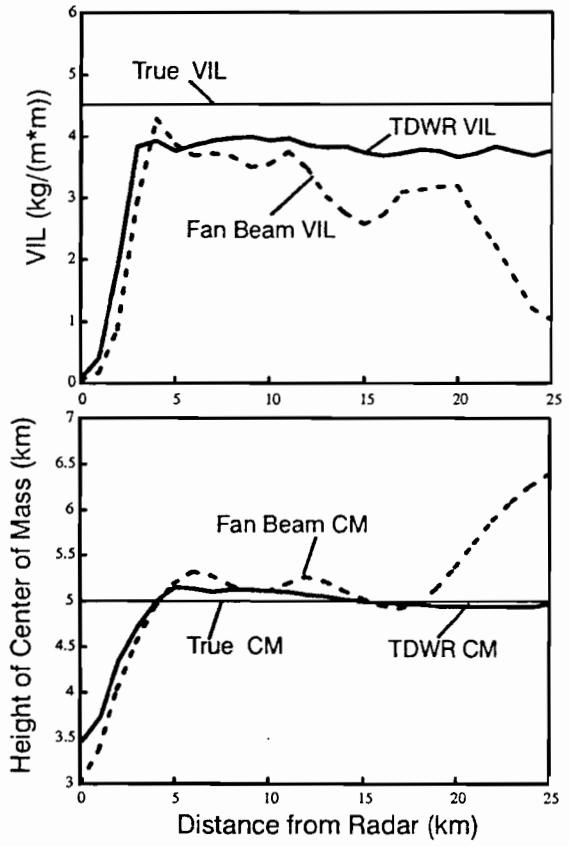

Figure 3. Apparent VIL and height of CM of model ellipsoid scanned with TDWR and fan beam strategies.

tion. We discovered that there was very little difference between 0.1 km and 0.5 km for the TDWR scan (Fig. 4). At 1.0 km, the measured parameters were still very close to their 0.1 km values, but the variability of CM with range increased. The ITWS prototype Microburst Prediction algorithm currently uses 1 km resolution (although 0.5 km vertical resolution is being considered), and the gridded Terminal Winds product uses 2 km horizontal resolution at 50 mb height intervals.

5. SUMMARY AND CONCLUSIONS

We have considered here the key unmet needs in the airport terminal area of adequate coverage both in time and space for detection and prediction of hazardous weather cells. Because thunderstorms evolve on such rapid time scales, this requirement may be a driver for the design of any new terminal weather surveillance system. It is our contention that requirements for update rate and spatial resolution must be developed in the context of likely use of the data – in gridded prediction systems, data assimilating numerical models, and for specific improvements in flight route planning, weather avoidance, and terminal air traffic capacity and efficiency.

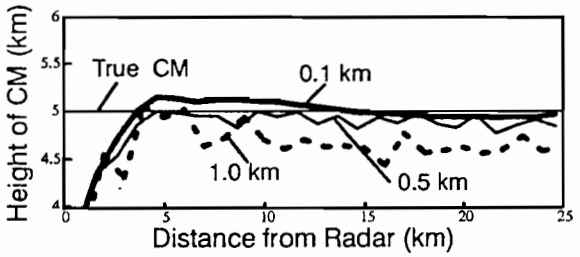

Figure 4. Apparent height of center of mass of model ellipsoid scanned with TDWR strategy, and gridded at 0.1, 0.5, and 1.0 km resolution. A 1.0 km interpolation radius was used at each resolution.

We have developed a methodology towards quantifying the weather surveillance requirements for update rate and coverage of convective storms. By making special radar measurements at high volume update rates, and comparing them with derived lower update rate scans, the benefit with respect to some detection or prediction algorithm or model can be quantified. Likewise, by sampling idealized or actual high resolution numerical model data of storms, trade-offs on required coverage resolution can be made. Based on these studies and other research performed at Lincoln Laboratory for the TDWR and ITWS programs, we can draw several conclusions.

1. Whole volume coverage to at least 4 km altitude in the terminal area is required every 1.0–2.5 min. The actual selected update rate will depend on the perceived cost/benefit ratio. State-of-the-art algorithms and numerical models should be used to calculate this ratio.

2. A "cone of silence", i.e. an unscanned region over the radar, is not acceptable over the airport.

3. Surface updates of 0.5–1.0 min are required over the airport and approach/departure corridors for timely outflow detection.

4. High resolution data (100–250 m range gate spacing, 1–1.5° azimuthal resolution) are required in the boundary layer, i.e. the lowest ~2 km. Contiguous beam coverage is desirable since wind speed changes rapidly with height near the surface. It is crucial to determining new areas of convection that boundary layer forcing (convergence) be adequately measured, and this requires low altitude coverage even at the far ranges of the terminal area.

5. Above ~2 km, resolution requirements can be relaxed. Wider beam widths can be tolerated, but the desired resolution at long range must still be taken into account.

ACKNOWLEDGEMENTS

We thank Margita Liepins, Barbara Forman, and Richard DeLaura for developing code for the analyses and simulations reported here, and their assistance in performing these studies.

REFERENCES

Andrews, J. and J. Welch, 1989: The challenge of Terminal Air Traffic Control Automation. Proceedings, *34th Air Traffic Control Association Conference*.

Carbone, R. E., M. J. Carpenter, and C. D. Burghart, 1985: Doppler Radar Sampling Limitations in Convective Storms. *J. Atmos. Oceanic Technol.*, vol. 2, num. 3, 357–361.

Evans, J. 1991a: Baseline weather prediction/detection systems. *FAA TASS Briefing to Industry*, Arlington, VA, B28–B42.

Evans, J. 1991b: Integrated Terminal Weather System (ITWS). Preprints, *4th Conference on Aviation Weather Systems*, Paris, Amer. Meteor. Soc., 118–123.

Keeler, J., 1991: Advanced observation concepts. *FAA TASS Briefing to Industry*, Arlington, VA, D42–D64.

McCarthy, J., 1991: Future weather concepts for terminal area surveillance.. *FAA TASS Briefing to Industry*, Arlington, VA, D3–D21.

Mueller, C., and J. Wilson, 1993: Rules for short-term forecast of thunderstorm initiation, evolution and movement: Procedures and automation. Preprints, *26th International Conference on Radar Meteorology*, Norman, Amer. Meteor. Soc., this volume.

Sherretz, L. 1991: Developing the Aviation Gridded Forecast System. Preprints, *4th International Conference on Aviation Weather Systems*, Paris, Amer. Meteor. Soc., 102–105.

Weber, M., M. Wolfson, D. Clark, S. Troxel, A. Madiwale, and J. Andrews, 1991: Weather information requirements for terminal air traffic control automation. Preprints, *4th International Conference on Aviation Weather Systems*, Paris, Amer. Meteor. Soc., 208–214.

Wilson, F. W., R. Cole, and J. McGinley, 1993: ITWS terminal gridded analysis. Preprints, *5th Conference on Aviation Weather Systems*, Vienna VA, Amer. Meteor. Soc.

Wolfson, M., R. Delanoy, M. Liepins, B. Forman, and R. Hallowell, 1993: The ITWS Microburst Prediction Algorithm. Preprints, *5th Conference on Aviation Weather Systems*, Vienna VA, Amer. Meteor. Soc.

A MACHINE INTELLIGENT GUST FRONT ALGORITHM FOR DOPPLER WEATHER RADARS

Richard L. Delanoy and Seth W. Troxel

Lincoln Laboratory, Massachusetts Institute of Technology
Lexington, MA 02173–9108 USA

1. INTRODUCTION

Gust fronts generated by thunderstorms can seriously affect the safety and efficiency of airport operations. Lincoln Laboratory, under contract with the Federal Aviation Administration (FAA), has had a significant role in the development of two Doppler radar systems that are capable of detecting low–altitude wind shears, including gust fronts, in the airport terminal control area. These systems are the the latest generation Airport Surveillance Radar, enhanced with a Wind Shear Processor (ASR–9 WSP) and the Terminal Doppler Weather Radar (TDWR).

Gust fronts produce signatures that are observable to varying degrees in reflectivity and Doppler velocity data generated by these radars. In Doppler velocity images, gust fronts are recognizable as zones of converging winds. In reflectivity images, gust fronts appear as thin lines of increased intensity, which occur as the result of rain, dust, insects, or debris being lofted and concentrated at the leading edge of the front. An existing automated gust front detection and forecasting algorithm, developed principally for TDWR data and called in this paper the Advanced Gust Front Algorithm (AGFA), has achieved respectable levels of performance using these data (Eilts, 1991 and Merritt, 1989). With clear, unambiguous radar signatures AGFA performs reasonably well. The challenge is in constructing an algorithm that can detect marginally detectable, ambiguous cases without incurring unacceptable false alarm rates.

Several sources of ambiguity exist. For example, gust front thin–line signatures can be obscured by large areas of precipitation. Velocity convergence signatures can vanish when gust front orientations result in bad Doppler viewing angles. Gust front signatures can also be mimicked by other natural phenomena, such as flocks of birds, clouds of dust stirred up at construction sites, elongated low–intensity rain echoes, and ground clutter. Finally, gust fronts can have very low radar cross–section densities, sometimes below the sensitivity of the radar system, making detection difficult.

The ASR–9 WSP provides a less expensive alternative to the TDWR as a terminal weather radar (Weber, 1989). Although not originally intended for weather imaging, this fan–beam Doppler radar generates images of sufficient quality that gust fronts can be identified and tracked. However, versions of AGFA adapted for ASR–9 WSP data have performed poorly. The primary reason for the lack of performance is the reduced gain and lowered sensitivity inherent in the fan–beam design of the ASR–9. With lowered sensitivity, clear air velocity estimates are unreliable. Consequently, few wind convergence signatures are visible, forcing AGFA to rely on only the thin–line portion of its algorithm. Unfortunately, the reduced sensitivity also makes faint thin–line signatures more fragmented and harder to resolve from background.

The radars themselves are sufficient for the task of gust front detection, since experienced human observers can detect and track gust fronts in images generated by these radars. And yet, sufficiently high detection rates with few false alarms has been an elusive goal for developers of automated gust front detection algorithms. Skilled human interpreters rely upon spatial and temporal contextual information and assimilate weak, uncertain, ambiguous, and even contradictory evidence. Humans are also adept at conditionally fusing information from various sources, reflecting knowledge that different signatures can have varying reliability that depends on situational context. In contrast, such traits of perceptual intelligence have been notoriously and surprisingly difficult to implement in computer vision systems.

2. ALGORITHM DESCRIPTION

A general–purpose approach to object recognition, which was originally developed in the context of automatic target recognition (ATR), has been incorporated in a Machine Intelligent Gust Front Algorithm (MIGFA). Use of the term "machine intelligence" in particular reflects the use of two new techniques of knowledge–based signal processing.

The first technique, functional template correlation (FTC) (Delanoy, 1992) is a generalized matched filter incorporating aspects of fuzzy set theory. For comparison, standard 2–D cross correlation relies upon a kernel that is essentially a subimage consisting of expected image values. In contrast, the kernel of a functional template consists of a set of integers that each correspond to a unique scoring function. Each scoring function, given an image value as input, returns a score reflecting how well that image value matched expectations for a given location on the kernel. The results of all scoring functions within the functional template are then averaged, resulting in a score in the range [0,1].

By increasing or decreasing the interval over which affirming scores (i.e., > 0.5) are returned, scoring functions can encode varying degrees of uncertainty with regard to what image values are allowable. But in addition, knowledge of how a feature or object appears in sensor imagery can be encoded in scoring functions. With various design strategies, the interfering effects of occlusion, distortion, noise, and clutter can be minimized. As a consequence, matched filters

*The work described here was sponsored by the Federal Aviation Administration. The United States Government assumes no liability for its content or use thereof.

customized for specific applications using FTC are generally more robust than traditional signal processing operations. The output of FTC is a map of values in the range [0,1], each of which reflects a belief that the shape or object implicitly encoded in a functional template is present at that image location. In our ATR systems, FTC has been used primarily as a direct, one-step means of 3-D object detection and extraction. In MIGFA, FTC is used for edge detection, thin-line filtering, thin-line smoothing, shape matching, and homotopic thinning of shapes.

The second major tool is the use of "interest" as a medium for data fusion and for assimilating evidence at the pixel level (Delanoy, 1991). An interest image is a map of evidence (values in the range [0,1]) for some feature that is selectively indicative of an object being sought (note that the output of FTC can be an interest image). Higher pixel values reflect greater confidence that the intended feature is present at that location. Given the assumption that the output of any feature detector can be configured as an interest image, evidence from any number of registered sources of information can be easily combined using simple or arbitrarily complex rules of arithmetic or fuzzy logic. Clusters of high values in the combined interest image are then used to guide selective attention and serve as the input for object extraction. In practice, we often use several weakly or inconsistently discriminating feature detectors to mutually support or compensate for each other, resulting in relatively robust performance.

The system block diagram in Fig. 1 illustrates the configuration of the ASR-9 WSP version of the system. Input images V (Doppler velocity image) and DZ (reflectivity image) are passed to six simple, independent feature detectors that use FTC.

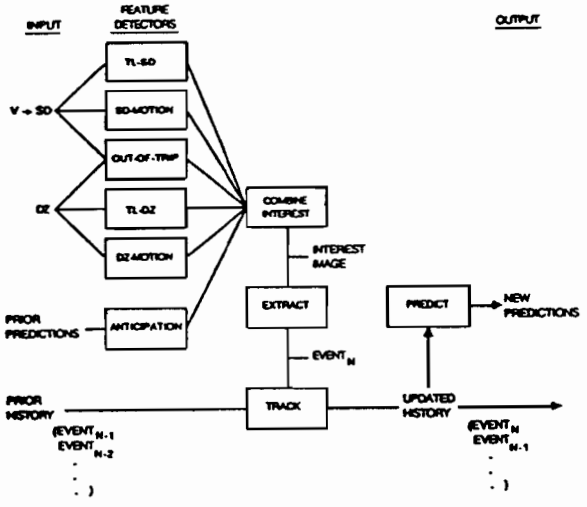

Figure 1. MIGFA block diagram.

The first one, marked TL-SD, uses an FTC filter for thin-lines in a map of local Doppler variance, called SD (standard deviation)[1]. A second feature detector, labelled SD-MOTION, applies a thin line filter to the difference of two sequential reflectivity images. Since differencing suppresses those signals that are stationary, the SD-MOTION detector tends to highlight only those thin-lines that are moving. The third feature detector, labelled OUT-OF-TRIP, uses FTC to identify range ambiguous echoes of more distant weather. Areas believed to reflect out-of-trip weather are given low interest values. The next two feature detectors, TL-DZ and DZ-MOTION perform the same kind of thin-line analysis as is done for TL-SD and SD-MOTION. The final feature detector, ANTICIPATION, will be discussed below. The outputs of the several feature detectors are combined as a weighted average to form a combined interest image.

From the combined interest image, fronts are extracted as chains of points. The chains extracted from a radar scan, collectively called an event, are integrated with the prior history by establishing point-to-point correspondence. Heuristics are applied at this point to reject chain points that have apparent motion that is improbable. The updated history is used to make predictions of where points along the front will be located at some future time. Such predictions are used in the processing of subsequent images, specifically in the feature detector called ANTICIPATION, which places high interest values wherever fronts are expected to be and by so doing selectively sensitizing the system to detecting gust fronts at specific locations. Anticipation is tuned so that it will not by itself automatically trigger a detection, but when averaged with other interest images will support weak evidence that would otherwise be insufficient to trigger a detection.

A second version of the gust front algorithm has been constructed for TDWR data, differing only in the set of feature detectors used. Differences in the TDWR detector set primarily reflect the greater dependence on Doppler data for finding areas of convergence.

3. RESULTS

A test set of ASR-9 WSP data collected in Orlando, Florida during AGFA field testing in 1991, contains 9 different gust fronts in a set of 450 images (15 hours). A human interpreter looking at the same ASR-9 WSP data detected 280 instances of the 9 gust fronts tracked by the radar. Four figures of merit are shown for each of the two algorithms. The probability of detection is the number of detections made by each algorithm as a percent of human-detected instances of gust fronts. The probability of false alarm (PFA) is the number of false alarms divided by the total number of algorithm detections. In addition to simply identifying fronts, the human interpreter delimited the length of each detected front. Detection quality was further assessed by comparing the length of the front as estimated by each algorithm against

1. Because measurements within gust front thin line have higher signal to noise ratios than the surrounding clear air measurements, gust fronts show up in SD as thin lines of lower signal variance.

that indicated by the human interpreter. The percent length detected (PLD) is the length detected expressed as a percent of the length delimited by the human interpreter. The percent of false length detected (PFD) reflects situations where the detected gust front lengths extended beyond what the human interpreter could see.

Table 1 compares performance of MIGFA against the previously constructed AGFA, which uses more conventional methods of signal processing and computer vision. The first two columns indicate that MIGFA, relative to AGFA, substantially increased the POD while decreasing the PFA. Similarly, the PLD reflects the improvement in detection rate. However, the increased PFD (from 13% to 33%) would suggest that MIGFA was doing a worse job of discriminating the extent of individual fronts. In order to better understand why MIGFA was extending fronts beyond what the human interpreter believed appropriate, we rescored AGFA and MIGFA results against human interpretations of TDWR data taken at the same time as the ASR–9 WSP data. We assume that truth derived from the more reliable TDWR data is more accurate than that for ASR–9 data. These results, shown in Table 2, confirm the general trend of the first 3 figures of merit shown in Table 1. However, now the PFD is quite low, essentially the same as that for AGFA. Consequently, these results, along with analyses of individual cases, leads us to believe that the MIGFA detected fronts were in fact more accurate than detections made by the human interpreter given the same ASR–9 WSP data.

Table 1. AGFA and MIGFA performance on ASR–9 WSP data as scored against human interpretations.

	Gust Fronts		Gust Front Length	
	POD	PFA	PLD	PFD
AGFA	56.7	4.6	38.9	12.9
MIGFA	88.1	0.6	86.2	33.4

Table 2. AGFA and MIGFA performance on ASR–9 WSP data as scored against human interpretations of matching TDWR data.

	Gust Fronts		Gust Front Length	
	POD	PFA	PLD	PFD
AGFA	42.6	3.2	21.0	4.2
MIGFA	75.1	0.0	58.7	6.4

This same version of MIGFA was installed on an ASR–9 WSP in Orlando, Florida for operational testing during the summer of 1992, the results of which are shown in Table 3. During the period from 1 August to 20 September, MIGFA correctly detected and tracked approximately 75% of all gust fronts identified by human interpreters examining ASR–9 WSP data. TDWR and anemometer data were also used for verification. Those gust fronts that were missed either had reflectivity levels near the sensitivity limits of the ASR–9 or were obscured by storm cells along the front. The false alarm rate was under 2%. Although TDWR–based truth has not yet been compiled for these data, an analysis of individual cases again indicates that the relatively high PFD (21%) consists largely of believable extensions of gust fronts that were not identified by the human interpreter.

Table 3. Results of MIGFA operational testing on ASR–9 WSP data collected in Orlando during summer 1992.

	Gust Fronts		Gust Front Length	
	POD	PFA	PLD	PFD
MIGFA	75.4	1.8	80.8	21.1

4. STATUS

MIGFA represents a substantial improvement in performance over previous efforts and is the prime candidate for deployment in production ASR–9 WSP systems. The TDWR version of MIGFA is scheduled for testing in summer 1993. Adaptations of the techniques used in MIGFA are currently being used, or are being considered, for other weather detection problems, including microburst prediction and sensor fusion.

REFERENCES

Delanoy, R.L., J.G. Verly, and D.E. Dudgeon, 1991: Pixel–Level Fusion Using Interest Images, *Proceedings of the 4th National Symposium on Sensor Fusion*, Orlando, FL, April 2–4, 1991.

Delanoy, R.L., J.G. Verly, and D.E. Dudgeon, 1992: Functional Templates and their Application to 3–D Object Recognition, *Proceedings of the 1992 International Conference of Acoustics, Speech, and Signal Processing*, San Francisco, CA, March 23–26, 1992.

Eilts, M.D, S. Olson, G. Stumpf, L. Hermes, A. Abrevaya, J. Culbert, K. Thomas, K. Hondl, and D. Klingle–Wilson, 1991: An Improved Gust Front Detection Algorithm for the TDWR, *Preprints, 4th International Conference on Aviation Weather Systems*, June 24–26, 1991, Paris.

Merritt, M. W., D. Klingle–Wilson, and S.D. Campbell, 1989: Wind Shear Detection with Pencil–Beam Radars, *Lincoln Laboratory Journal*, Vol. 2, No.3, 483–510.

Weber, M.E. and T.A. Noyes, 1989: Wind Shear Detection with Airport Surveillance Radars, *Lincoln Laboratory Journal*, Vol. 2, No. 3, 511–526.

DUAL–DOPPLER MEASUREMENTS OF MICROBURST OUTFLOW STRENGTH ASYMMETRY

Robert G. Hallowell

Massachusetts Institute of Technology Lincoln Laboratory
Lexington, Massachusetts

1. INTRODUCTION

The Federal Aviation Administration (FAA) has been sponsoring Lincoln Laboratory in its effort to develop and test weather detection algorithms for the Terminal Doppler Weather Radar (TDWR). An automated microburst detection algorithm (Merritt et al., 1989) operates on the TDWR radial velocity data and, based on the shear and velocity difference along the radial, outputs regions which are hazards to aviation. This algorithm has been operating since 1987 in Denver, Kansas City, and Orlando and is part of the operational TDWR being deployed across the country. One issue which continues to cause concern for automated windshear detection is microburst asymmetry. Asymmetry, or aspect angle dependence, in microbursts refers to outflows which have a divergent surface outflow strength or extent that varies depending on the viewing angle of the radar.

The TDWR is a single–Doppler radar, therefore, an asymmetric microburst may be underestimated or go undetected if the radar is viewing the event from an aspect angle where the strength of the outflow is weak. Past work by Wilson et al. (1984), Eilts (1987,1988), and Hallowell (1990) has indicated that some microbursts are highly asymmetric. Strength asymmetries (maximum/minimum strength over all viewing angles) from these past studies ranged from 1.3 to as high as 6.0. Hallowell (1990) using Denver data examined 27 Denver microbursts (96 observations) and found strength asymmetries from 1.3 to 3.8 with a median of 1.9. However, this previous work has been limited in scope to Denver and Oklahoma (plains) microbursts, and may have used assumptions about the data which introduce false or apparent asymmetry.

2. APPARENT ASYMMETRY

Previous investigators selected dual–Doppler microburst events using the following criteria:

- Intersection angle of beams between 30° and 150°
- Tilt times of the two radars within one minute
- Elevation angles of both radars less than 1.0°

In the course of studying microburst events, we have found that while these assumptions are valid for large scale, slow moving and developing wind fields, they are not sufficiently strict for microburst outflows. We utilized simulated three–dimensional velocity data of a symmetric microburst obtained using the WME (Wisconsin Model Engine) sub–cloud model (Anderson, 1992). Radial data were extracted from the simulated data from two hypothetical radars situated 15 km from the microburst center at various elevations angles, beam widths, times, and intersection angles. We then input these tilts in various combinations to gather data on how the apparent asymmetry of the event changed for each parameter. Using these model results we were able to quantify the effects of various dual–Doppler coordination parameters on the measured asymmetry of the real microburst data. The following base configuration was used (changes are noted in each sub–section): Fictitious radars located 15 km from microburst center at 90° beam intersection angles, 1.0° beam width, 0.4° elevation angles, and a gate spacing of 150 meters.

2.1. Dual–Doppler Process Itself

The wind synthesis process which operates on the smoothed polar radial velocity data and creates a two–dimensional Cartesian windfield grid introduces asymmetry of its own. By extracting two tilts of fictitious radar data at 90° angles and keeping all other parameters the same, we find a dual–Doppler microburst field which yields an asymmetry of 1.04. This apparent asymmetry has not been removed in the graphs that follow.

2.2. Horizontal Beam Intersection Angles

The angle of intersection between the radar radial data is extremely important in determining the quality of the dual–Doppler wind field. By holding all other parameters constant and changing only the intersection angle of the radars, we see from Figure 1 that intersection angles less than 45° yield increasing apparent asymmetry results.

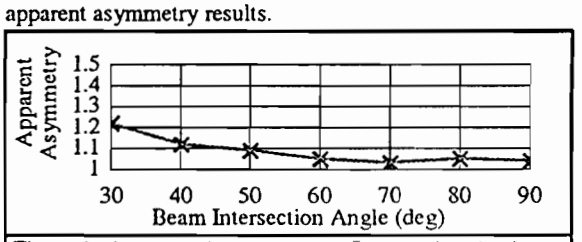

Figure 1. Apparent Asymmetry vs. Intersection Angle

2.3. Temporal Variations

The time between tilts is another key measure of data quality; in microbursts one minute can mean a change in strength of over 10 m/s. Looking at the observations, we find that 90% of the 1 minute changes in differential velocity are less than 7 m/s. The microburst model used has a peak differential velocity of 51 m/s and one minute prior to the peak a velocity of 44 m/s. By matching extracted tilts from different 15 sec time steps (with all other parameters the same), we find that data compared with 45 secs or less time differential yields very low apparent asymmetries (Figure 2). Care should be taken in applying this to all microbursts; rapidly developing or decaying

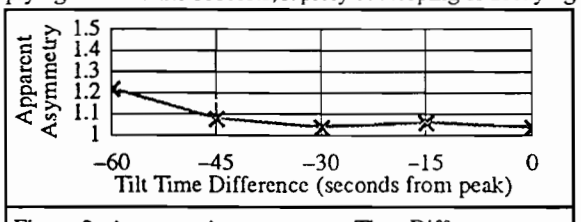

Figure 2. Apparent Asymmetry vs. Time Difference

*The work described here was sponsored by the Federal Aviation Administration. The United States Government assumes no liability for its content or use thereof.

microbursts will be more of a problem even in a 30 sec time interval.

2.4. Beam Width, Elevation Angle Differences

On examining these parameters separately it is difficult to discern a pattern. What we finally found was that the extent of vertical beam overlap was the important feature, not a specific beam width or elevation angle. By processing one tilt at 0.0° elevation and its tilt pair at increasingly higher elevation angles we find beam overlap to be the overriding concern for apparent asymmetry (Figure 3). The simulation used for this analysis

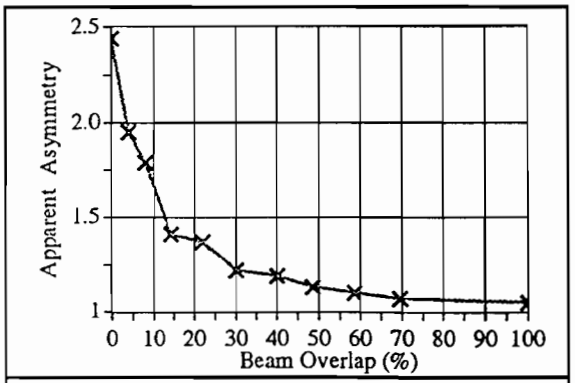

Figure 3. Apparent Asymmetry vs. Beam Overlap

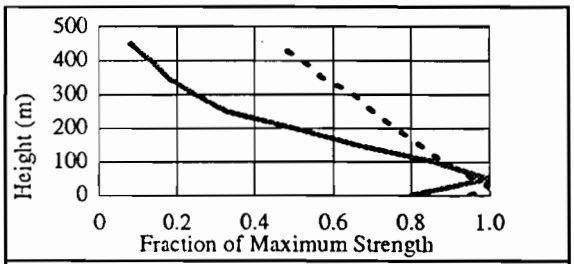

Figure 4. Vertical Strength Profile: Simulated (solid) & Measured (dashed)

was for a very strong microburst, and its vertical profile is steeper than that found by Biron and Isaminger (1991) for Denver microbursts. Figure 4 shows the vertical profile of both the simulated data (solid line) and the Denver observations (dashed line). While the overall simulated profile presents a worst case scenario, the lowest 200 m are fairly comparable, and this is where the 30% and greater overlap analysis was performed.

2.5. Recommendations

The following criteria were used in this analysis, and should be used by other researchers, to limit the affects of apparent asymmetry on asymmetry analyses:

- Intersection angles between 45° and 135°
- Tilt time differences < 30 secs, and
- Radar beam overlap by 50% or more, or beam centers within 50 m (this guarantees that each radar catches at least a portion of the other radar's center beam).

3. DATA

The data used were collected in Denver, CO (1988), Kansas City, MO (1989) and Orlando, FL (1990). At each site, there were two radars operating: the MIT/LL TDWR testbed radar (FL–2) and the University of North Dakota C–Band Doppler Radar (UND). FL–2 and UND both have one degree beams, FL–2 was an S–Band radar prior to 1990 but modified to C–Band in 1990. The radar scanning was coordinated to cover microbursts which occurred in favorable dual–Doppler regions. For each scan of an event, the two–dimensional surface wind field was calculated using the multiple Doppler radar synthesis system suggested by Brown et al. (1981). The raw two–dimensional wind fields were then smoothed once using a simple 3–by–3 median filter, with 4 of 9 points required to be valid.

Microbursts were selected by examining the two–dimensional windfield for divergence regions. This subjective examination process yielded over 1000 observations and some 100 events (multiple observations of the same microburst). Some observations, taken at the beginning or end of an event, were not true outflows and were removed from the analysis by dropping observations which had minimum differential velocities less than 3.5 m/s. With this restriction, a total of 859 observations of microbursts were examined for asymmetry; a breakdown by site is shown in Table 1.

Table 1.Breakdown by Site of Data Examined

	Days	Events	Observations
Denver	6	36	476
Kansas City	7	27	163
Orlando	4	22	220
Totals	17	85	859

4. METHODOLOGY

The methodology used to analyze microburst events from dual–Doppler is essentially the same as that detailed by Hallowell (1990). Briefly, an analyst examines the wind field and draws a polygon around a microburst outflow. Gridpoints of velocity data within the polygon are then intercompared to calculate velocity differences. Every gridpoint pair has its own orientation angle with respect to North (based on a fictitious radar 15 km from the event, see Figure 5), from which we can determine what the peak differential is at various orientation angles.

5. RESULTS

Three sites and 859 observations of microbursts were examined for this study. When the strict criteria from Section 2.5 are applied, we find a definite shift toward lower asymmetry as shown in Figure 6. The median asymmetry ratio for the re-

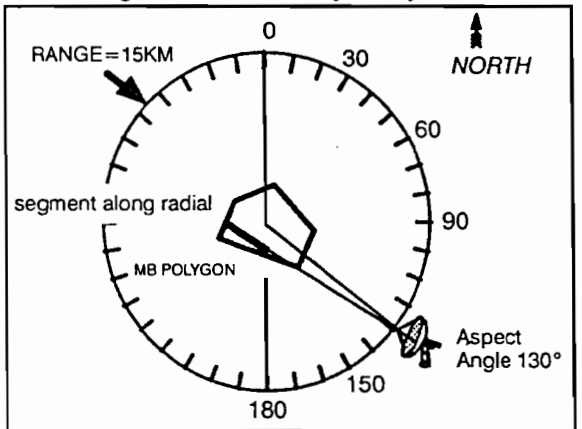

Figure 5. Diagram illustrating relative aspect angle calculations for asymmetry analysis.

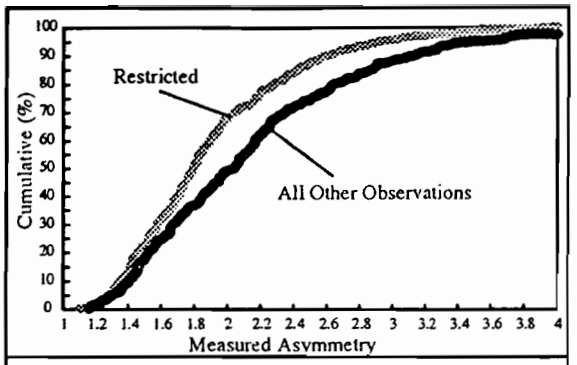

Figure 6. Percent Frequency of Asymmetry Ratios for Restricted (grey) and All Other Observations (black).

stricted set of data (498 observations) is 1.78 while all other observations have a median asymmetry over 2.0 (361 observations). By no means has all the apparent asymmetry been eliminated; restricting cases to remove all apparent asymmetry would leave no observations to work with. However, a reasonable estimate of the lowest possible real asymmetry curve can be made based on the known apparent asymmetry error left in the data. The measured asymmetry can be obtained by applying the following formula:

$$A_{measured} = A_{real} * A_{time\_diff} * A_{beam\_angle} * A_{overlap} * A_{dual}$$

This formula assumes a worst case scenario, where the asymmetries due to temporal variations (A_{time_diff}), beam intersection angles (A_{beam_angle}), elevation angle overlap ($A_{overlap}$), and the dual–Doppler process itself (A_{dual}) compound one another. Sometimes the apparent asymmetries may be oriented such that they actually counteract one another, although the test data studied indicates this is less likely. By restricting the data, I have attempted to limit the impact of each apparent asymmetry to under 5% for A_{dual}, A_{time_diff}, A_{beam_angle}, and to under 15% for $A_{overlap}$. By dividing the restricted measured asymmetry curve by our estimated error ($1.15 * 1.05^3 = 1.33$), I obtain a measure of the expected cumulative distribution of real asymmetry (Figure 7). The chart indicates the real asymmetry median could be as low as 1.34, but the actual answer likely lies between the two curves.

If we examine asymmetry on a site by site basis, we find that for each site the restricted data set yields lower asymmetries than unrestricted data (not shown). Figure 8 shows the cumulative distribution of asymmetry ratios for each of the three sites examined. Orlando and Denver turn out to have very similar distributions of asymmetry, with medians of 1.72 and 1.76, respectively. Kansas City shows a tendency toward higher asymmetry (median 1.9), however 1989 was an atypical climatological year there. Because of this, the quality and quantity of the data collected in Kansas City may have been insufficient to make any firm conclusions about midwest microbursts.

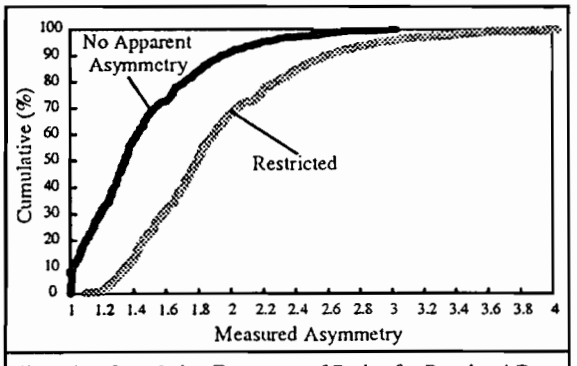

Figure 7. Cumulative Frequency of Ratios for Restricted Data: Measured (grey) and No Apparent Asymmetry (black).

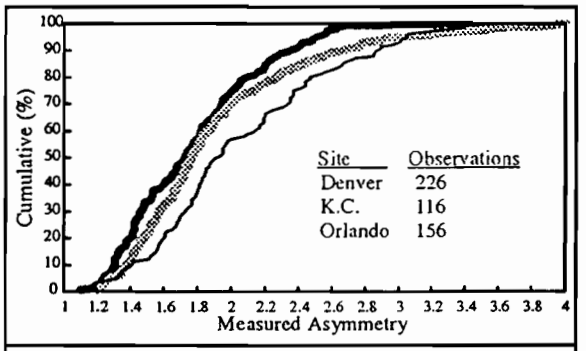

Figure 8. Cumulative Frequency of Ratios for Restricted Data: Denver (grey), Kansas City (thin black), and Orlando (thick black).

6. CONCLUSIONS

Previous studies of microburst asymmetry have not considered the impact of radar configurations, thereby, introducing apparent asymmetry into the analysis. By using simulated data we are able to estimate the impact of temporal difference, vertical beam overlap, and horizontal beam intersection angle factors in processing and analyzing dual–Doppler microburst events. A total of 859 microburst observations were examined from three geographical regions. We find that overall asymmetry distributions are lower than had been found in all previous studies, and that differences in asymmetry between sites such as Orlando and Denver are minimal. Overall, the measured asymmetry ratios in the observation data vary from 1.1 to 4.0 (with less than 5% over 3.0) and have a median value of 1.78. In addition, estimating and removing the residual errors of apparent asymmetry from the observation data set yields a distribution of 1.0 to 3.0 and a median of 1.34.

ACKNOWLEDGEMENT

I would like to thank John Anderson at the University of Wisconsin for the simulation data which was extremely helpful in illuminating the apparent asymmetry phenomena.

REFERENCES

Anderson, J., et al.., 1992: A 3–D Model System for Simulating Thunderstorm Microburst Outflows. *Journal of Meteorology and Atmospheric Physics*, vol. 49, pp.125–131.

Biron, P., and Isaminger, M., 1991: High Resolution Microburst Outflow Vertical Profile Data from Huntsville, Alabama and Denver, Colorado Project Report, *MIT Lincoln Laboratory*, ATC–163.

Brown, R., et al., 1981: Multiple Doppler radar analysis of severe thunderstorms: designing a general analysis system. NOAA Technical Memorandum ERL–NSSL–92.

Eilts, M., 1988: Use of a single Doppler radar to estimate the runway to wind shear component in microburst outflows. 26th Aerospace Sciences Meeting Paper, Jan., 1988, *American Institute of Aeronautics and Astronautics*, AIAA–88–0694.

Eilts, M., and Doviak, R., 1987: Oklahoma downbursts and their asymmetry. *Journal of Climate and Applied Meteorology*, vol. 26, pp. 66–78.

Hallowell, R., 1990: Aspect Angle Dependence of Outflow Strength in Denver Microbursts: spatial and Temporal Variations. Preprints, 16th Conference on Severe Local Storms, Kananaskis Park, Alta., Canada, *American Meteorological Society*, pp. 397–402.

Merritt, M., et al., 1989: Wind shear detection with pencil–beam radars. *The Lincoln Laboratory Journal*, Volume 2, Number 3, pp. 483–510.

Wilson, et al., 1984: Microburst wind shear and evaluation of Doppler radar for airport wind shear detection. *Journal of Climate and Applied Meteorology*, vol. 23, pp. 898–915.

A SHEAR-BASED MICROBURST DETECTION ALGORITHM FOR THE INTEGRATED TERMINAL WEATHER SYSTEM (ITWS)

Timothy J. Dasey

MIT/Lincoln Lab
Lexington, Massachusetts

1. INTRODUCTION

Microbursts are small scale, low altitude wind shear phenomena which have been associated with many recent aircraft accidents. Microbursts arise from thunderstorms and are characterized by intense downdrafts which spread out after impacting the earth's surface and display strong divergent outflows of wind. They are usually associated with heavy rainfall (Wolfson, 1988).

The Terminal Doppler Weather Radar (TWDR) program was the first attempt at microburst detection with a ground-based radar in the airport terminal area. Improving safety was its primary goal, and test operations in Denver, Kansas City, and Orlando have shown it highly successful in identifying microbursts. In general, this identification has been performed with a > 90% Probability of Detection (POD) and a < 10% Probability of False Alarm (PFA) (Campbell and Olson, 1987).

The Integrated Terminal Weather System (ITWS) seeks to enhance this ability. Microburst Predictions will be produced in addition to detections (Wolfson et. al., 1993). A microburst trend product, giving predictions of increasing microburst intensity along runway corridors over short time periods (2-3 minutes), is to be introduced. This microburst trend product will involve the ability to predict the future location, size, and intensity of the microburst. It is largely due to the microburst trend product that the philosophy behind microburst detection is being revised.

Although the TDWR algorithm is successful in detecting the area(s) of hazard, the output representation is not suited for tracking microbursts. The ITWS algorithms attempts to alleviate this by providing one output shape for each downdraft. The TDWR alerting is fundamentally loss based, that is, the severity of the hazard is indicated by the strength of the surface divergence couplet. However, if this divergence is not over a small area, an aircraft will experience little or no performance deficit. The ITWS algorithm captures this information by examining the divergence shear (rate of change in velocity) as well as the loss. Ground-based doppler radar observation has shown, and instrumented aircraft penetrations have confirmed (Matthews and Berke, 1993, Campbell et. al., 1992). that the shear within a microburst is highly nonuniform. The ITWS algorithm will use an additional, imbedded warning shape to indicate especially hazardous regions of a microburst.

This paper explains the initial design of the ITWS microburst detection algorithm and illustrates some early results. The final section concentrates on the testing plans for algorithm testing and the intended enhancements to its capabilities.

2. ALGORITHM DESIGN

The algorithm is comprised of four primary elements: radial shear calculation, segment formation, region formation, and alarm generation. The algorithm is intended to find microbursts, and weaker wind shear events, out to a 30.0 km range, but 35.0 km is actually processed to alleviate edge effects. Surface scans from the TDWR are available approximately every minute. The ITWS microburst algorithm will process all scans equal to, or below 1.0 degrees elevation angle.

The radial shear is calculated as the spatial derivative of the radial velocity field. The base velocity data is first median filtered, using a range adaptive filter size (approximately 1km by 1km), and a least squares fit of a line segment to the data is performed as in Figure 1. The slope of the fit line segment is written as the radial shear at that gate. Both the median filtering and the regression fitting output a valid value only if at least a certain percentage (currently 50%) of base velocity values are valid.

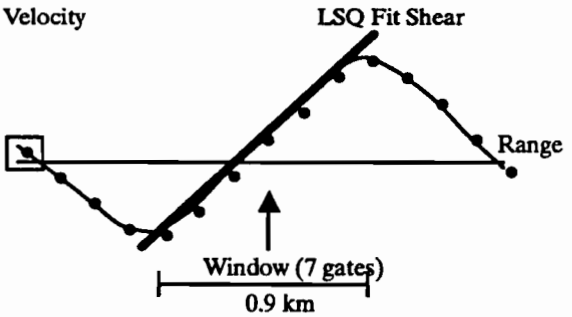

Figure 1. Illustration of shear calculation. The slope of the heavy line is assigned as the shear value.

The segment forming module processes the radial shear map to locate contiguous segments along a radial above

*The work described here was sponsored by the Federal Aviation Administration. The United States Government assumes no liability for its content or use thereof.

a set of user defined thresholds. Currently, two thresholds, 5.0 m/s/km (low shear) and 10.0 m/s/km (high shear) are used. The segment must meet a minimum length to be considered valid. Each valid segment is then extended until either (a) the average shear along its length falls below the threshold, (b) a gate with a negative shear value is encountered, or (c) an excessive number of consecutive invalid shear values are found. In this way, a segment is not considered unless a minimum shear is present, but the length of the segment is not rigidly tied to the points above threshold. The loss (velocity difference) across the segment is calculated over a different scale, found as the maximum segment length while the average shear remains above 2.5 m/s/km, or until conditions (b) or (c) are found.

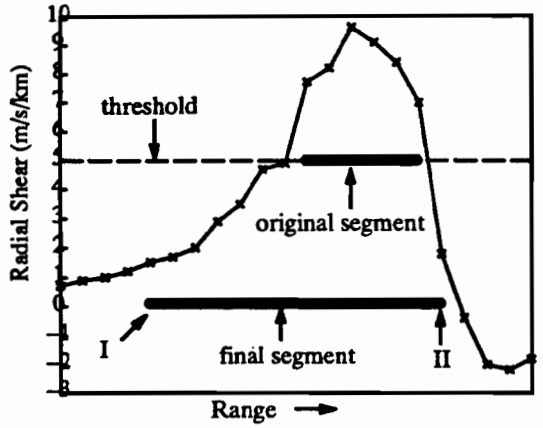

Figure 2. Depiction of Segment forming process. The final segment endpoint I was placed by condition (a), and endpoint II was placed by condition (b).

The Region formation module processes the set of shear segments at each threshold level into regions of high shear. Regions are built by associating segments on adjacent radials which overlap by a user defined percentage. A circular shape is fit to the segments of the region using an optimization technique. The parameters of the circle (x–center, y–center, radius) are altered to minimize the sum of the minimum distance from each segment end to the circle perimeter and the distance of the segment end to the circle center. The optimization is unidimensional (each parameter is optimized one at a time), since it was determined that the extra computation for a multidimensional technique was not necessary. The region is discarded if a minimum number of segments is not included or if the area of the best fit circle is below a threshold. Regions from the high and low shear threshold levels are associated together if the percent area of intersection is higher than a user–defined amount. Those high shear regions without an accompanying low shear region are discarded.

The low shear regions are passed through a final alarm generation test. If the maximum loss from any segment in a region is greater than 30 knots and the peak shear within the region is greater than 10.0 m/s/km, a microburst alert is generated. If the maximum loss exceeds 15 knots and the peak shear is greater than 5.0 m/s/km, a wind shear alert is generated. All high shear regions associated with the alarm regions are also output for display.

3. RESULTS

The algorithm has thus far been executed on 12 microburst cases, using TDWR testbed data collected from Orlando (8 cases), Kansas City (2 cases), and Denver (2 cases). On this data set it has demonstrated that it can at least match the performance of the TDWR algorithm in identifying microbursts and quantifying their intensity. Additional studies are necessary to ensure that the false alarm rate is also comparable.

The additional goals of a more accurate downdraft identification and output shape consistency as an aide to tracking have produced mixed results. Isolated events, such as that shown in Figure 3, 4, and 5 are successfully characterized as originating from single downdrafts. As a result, the algorithm is successful in assigning event labels and following a consistent track over the lifetime of the event. Situations with multiple, interacting downdrafts are currently identified more erratically. This originates from an improper identification of the downdrafts, and results in difficult to interpret apparent merges and splits of events. Recent evidence about the correlation between peak shear locations and downdrafts, and additional aloft information which will be integrated from the ITWS Microburst Prediction algorithm (Wolfson et. al., 1993) indicate that this problem can be alleviated in the short term.

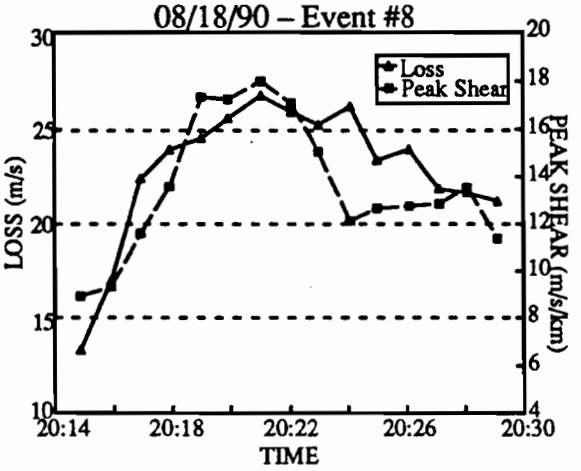

Figure 3. The loss and peak shear values over the course of an Orlando, 1990 microburst, as determined by the ITWS Microburst Detection algorithm.

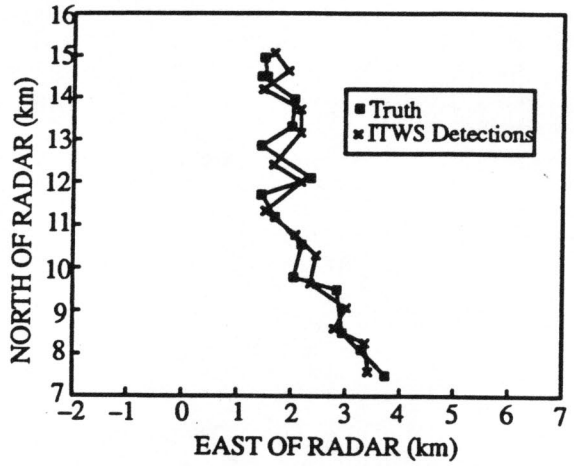

Figure 4. The location track of the same microburst event as in Figure 3. The center of the circle output by the ITWS algorithm is used as the location, and the truth has been determined by hand by an expert meteorologist.

4. FUTURE DIRECTION

The ITWS algorithm will be tested in real–time in the ITWS testbed site in Orlando, Florida from 5/93 through 9/93. This is expected to give us a large dataset for the inevitable modification and fine tuning of the algorithm. The ITWS Microburst Prediction and Microburst Trend algorithms will also be running in Orlando, beginning 7/93. This will help examine the strong interactions between the algorithms.

There are several enhancements to the algorithm which are expected to be made in the next calendar year. Other sensors are to be examined, particularly the Low Level Wind Shear Alert System (LLWAS), for integration with the ITWS algorithm. This will ensure that a consistent single alert is made for the entire terminal area. Attempts will be made to compensate for microburst asymmetry and adjust for aircraft altitude in microburst intensity warnings. Aloft information, of the kind the ITWS Microburst Prediction algorithm is considering (Wolfson et. al., 1993), will be used to provide a more accurate identification of the strength and location of the downdraft. This is important, since the vertical winds are not captured by low elevation angle ground based radar scans, and the downdraft is also a source of significant hazard for an aircraft.

REFERENCE

Campbell, S. D., Berke, A. J. and M. P. Matthews, 1992: Orlando TDWR Testbed Results. Proc. Fourth Combined Manufacturers and Technologists' Airborne Wind Shear Review Meeting.

Campbell, S. D. and S. H. Olson, 1987: Recognizing Low–Altitude Wind Shear Hazards from Doppler Weather Radar: An Artificial Intelligence Approach. J. Atmospheric and Oceanic Technology 4(1): 5–18.

Matthews, M. P. and A. J. Berke, 1993: Estimating a Wind Shear Hazard Index from Ground Based Terminal Doppler Radar. This volume.

Wolfson, M., 1988: Characteristics of Microbursts in the Continental United States. The Lincoln Laboratory Journal 1(1): 49–74.

Wolfson, M., Delanoy, R., Leipins, M., Forman, B., and R. Hallowell, 1993: The ITWS Microburst Prediction Algorithm. Proc. 5th Conference on Aviation Weather Systems, Vienna, Va. In Press.

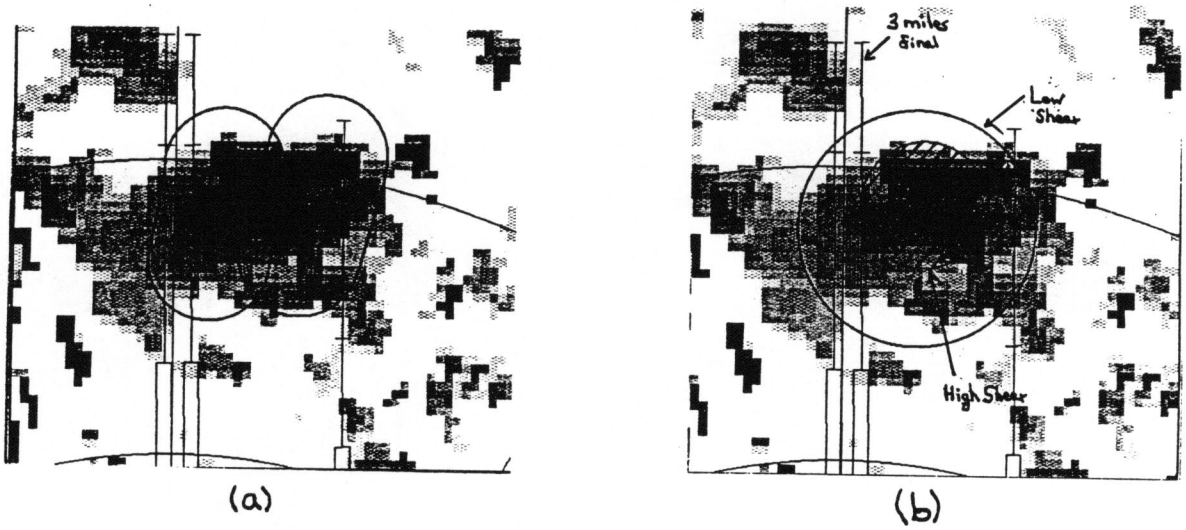

Figure 5. Comparison of (a) TDWR and (b) ITWS algorithm shapes for time 20:17 in the event of Figure 3 and 4. A high shear region is cross–hatched within the outer ITWS shape.

ESTIMATING A WINDSHEAR HAZARD INDEX FROM GROUND–BASED TERMINAL DOPPLER RADAR *

Michael P. Matthews and Anthony J. Berke

M.I.T. Lincoln Laboratory
Lexington, Massachusetts 02173
Telephone: 617/981–3547, E–mail: mpm@ll.mit.edu

1. INTRODUCTION

In the past decade, a great deal of effort has been invested in developing ground–based wind shear detection systems for major U.S. airports. However, there has been a lack of research in developing a quantitative relationship between the wind shear hazards detected by ground–based systems and the actual hazard experienced by an aircraft flying through the affected air space. To date, the main thrust of the verification efforts for ground–based systems has been to ensure that the system accurately detect and report the presence of the meteorological phenomena that cause potentially hazardous windshear. There is a subtle, but potentially important difference between detecting the presence of a microburst and detecting the presence of an aviation hazard. With this in mind, it would seem prudent to rigorously determine what correlation exists between the wind shear warnings that are generated from ground systems and the performance impact on aircraft flying through the impacted airspace. The operational demonstration of the testbed Terminal Doppler Weather Radar (TDWR) in Orlando, Florida along with the testing of airborne Doppler radar systems created a unique opportunity to compare extensively the ground–based windshear reports with in–situ aircraft measurements.

This paper presents the results from 69 microburst penetrations flown in 1990 and 1991 by the University of North Dakota (UND), the National Aeronautics and Space Administration (NASA) Langley Research Center, and Rockwell Collins under surveillance of the Lincoln–operated TDWR testbed radar. The primary goal of the research was to determine the relative accuracy of several methods designed to generate a numerical microburst hazard index, called the F factor, from ground–based Doppler radar data. It is hoped that this work will provide both a qualitative and quantitative basis for the discussion and assessment of microburst hazard reporting for ground–based microburst detection systems.

The Integrated Airborne Wind Shear Program is a joint NASA/Federal Aviation Administration (FAA) program with the objective to provide the technology base that will permit low altitude windshear risk reduction through airborne detection, warning, and avoidance. Additionally, the program aims to demonstrate the practicality and utility of real–time assimilation and synthesis of ground–derived windshear data to support executive level cockpit warning and crew–centered information display. Lincoln Laboratory joined this effort and provided the weather radar ground support and some of the post–flight data analysis for NASA's microburst penetration flights in Orlando, Florida.

*The work described here was sponsored by the National Aeronautics and Space Administration. The United States Government assumes no liability for its content or use thereof.

2. F FACTOR EQUATION

Currently, ground–based and airborne windshear sensors characterize the microburst hazard in two different ways. Airborne systems characterize the hazard in terms of F factor(Bowles, 1990), a volumetric parameter that measures the rate of change of aircraft energy. Ground–based systems such as TDWR report the strength of the windshear event as a single number representing peak point–to–point loss. Therefore, it was necessary to process the radar base data to compute the F factor for each penetration. This was accomplished by two methods. The first method involved using the TDWR algorithm loss estimate and the second involved a shear calculation from the radial velocity data. Both methods used a Lincoln modified version of the F factor equation proposed by Roland Bowles of NASA Langley Research Center (Bowles, 1990):

$$F_T = K' \frac{\Delta V}{\Delta R}\left(\frac{GS}{g} + \frac{2h}{GS}\right) = F_h + F_v \qquad (1)$$

where K' is a constant, ΔV is the velocity difference, ΔR is the distance over which the velocity difference occurred, GS is the groundspreed of the aircraft, and h is the height of the radar beam. The F factor equation is composed of two terms, the horizontal term(F_h, effect of headwind/tailwind loss on the aircraft), and the vertical term(F_v, effect of the downdraft on aircraft performance). The Doppler radar is only capable of measuring the wind component along a radial, therefore, the aircraft generally flew flight paths along a radial. This compensated for inconsistences between radar and aircraft measurements in the horizontal term, however, some method was needed to estimate the vertical term from the Doppler data. This was done by employing a simplified model of the mass continuity equation. The outflow region is viewed as a cylinder with the height of the radar beam acting as the top of the cylinder. Because the ground acts as a cap preventing flow out the bottom, what flows into the top (i.e. downdraft) must exit through the sides of the cylinder as horizontal outflow. With this model, the outflow is directly proportional to the downdraft depending upon the radius of the cylinder and the deceleration profile of the downdraft with height.

3. ESTIMATION OF F FACTOR USING TDWR ALGORITHM OUTPUT

The TDWR microburst algorithm defines a microburst outflow region by fitting a race track shaped icon around

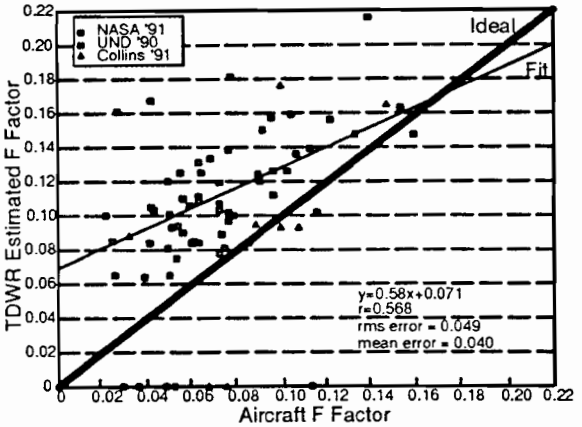

Figure 1 TDWR algorithm output vs. aircraft total F factor.

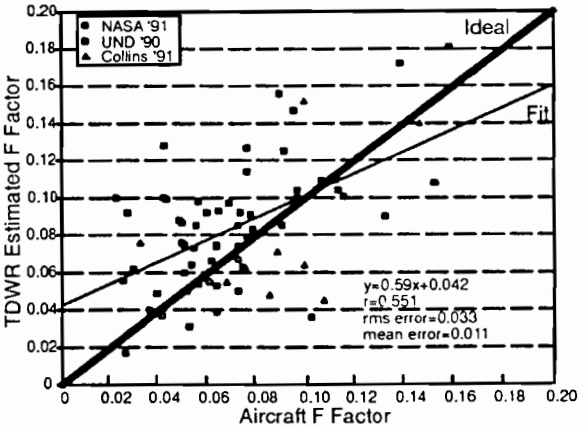

Figure 2 TDWR shear map vs. aircraft total F factor.

groups of radar radial velocity segments that show sufficient shear along their length. Site adaptable parameters control the maximum size of a shape, the minimum shape radius, and other shape characteristics. Each icon is assigned a value denoting the peak-to-peak velocity difference contained within the shape. This ranged from the largest to the second largest segment ΔV depending upon the number of segments contained within the shape. This peak-to-peak velocity difference was taken to be the ΔV term of equation (1), and the ΔR term was based upon the 85th percentile shear within the shape.

For each of the 69 microburst penetrations, an F factor was calculated from the output of the Lincoln version of the TDWR microburst algorithm using the techniques described above. Figure 1 is a plot of the TDWR estimated total F factor (TDWR F_T), compared to the *in situ* F factor. From the figure it can be seen that the computed TDWR F_T was consistently higher than the *in situ* F factor. Most notable is that the estimation was biased especially high for the NASA events.

The unexpectedly high values of TDWR F_T may be due to several factors, the most obvious of which is that the F factor computed from the microburst alarms assumes that the shear has a constant value at all points within the alarm's boundary. This assumption is incorrect, and since the aircraft sampled only a small portion of the area enclosed by the microburst alarms, it is quite possible that on many occasions they missed the localized "hotspot" of shear that caused the large value reported by the TDWR. The test pilots indicated during interviews that they occasionally avoided the most severe portion of a storm intentionally due to flight safety considerations.

4. ESTIMATION OF F FACTOR USING TDWR SHEAR MAP

F factors can be computed from the TDWR testbed's radial velocity data by creating a map of the radial shear. To do this, the radar base data were first subjected to a data quality editing process and then velocity dealiasing. The data quality editing consisted of clutter removal, point-target editing, and range obscuration editing. Next, the velocity field was median filtered using a sliding window of approximately 500 meters x 500 meters. The actual radial shear computation for each range gate was made by performing a least squares fit on seven gates centered about the point. With the TDWR radar's 150 meter gate spacing, this resulted in a fit over a radial distance of 1050 meters. This general method of shear computation is similar to work done by Britt(1992) for NASA's airborne Doppler windshear detection system.

The F factor can then be estimated along the trajectory of the aircraft by using the closest radial shear value as calculated from the TDWR base data. Figure 2 shows the peak total F factor as estimated from the TDWR shear map versus the peak total *in situ* F factor. A comparison with Figure 1 shows improved agreement between the TDWR and *in situ* F factor at the expense of an increased incidence of underestimation. Examination of the significant cases of underestimation reveals that in nearly all cases the error was due to the aircraft encountering a large downdraft that was not predicted by the shear map F factor calculation.

5. COMPARISON OF AIRCRAFT AND RADAR ESTIMATES OF HORIZONTAL F FACTOR

As mentioned in Section 3, it is useful to look at the horizontal and vertical terms of the F factor when attempting to analyze the success and failure of the various estimation techniques. From equation 1, the horizontal term can be calculated directly from the TDWR shear map data using the following formula (Note: K' is equal to one because the shear map is a one kilometer shear):

$$F_H = \frac{\Delta V}{\Delta R}\left(\frac{GS}{g}\right) \qquad (2)$$

Figure 3 compares the horizontal term of the F factor as estimated from the TDWR shear map and the aircraft. The shear map provides a fairly good estimate of the horizontal F factor, but tends to overestimate. A possible explanation for an overestimated F factor from the shear map is the difference between the altitude of the aircraft and the radar beam. For most of the events, the aircraft penetrated the microburst at a much higher altitude than the radar beam. Physical observations and modeling results suggest that the horizontal shear in a microburst varies with altitude. Thus, it would seem prudent to attempt to compensate for the discrepancy between the height at which the TDWR antenna beam and the aircraft measured the microburst intensity.

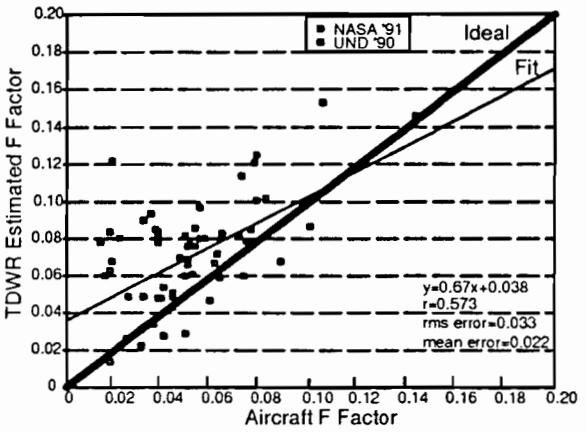

Figure 3 Shear map vs. aircraft horizontal F factor at F total peak time.

The Vicroy(1991) analytical microburst model includes a vertical shaping function for the horizontal wind velocity that is a good fit to experimental data. Correcting for altitude, Figure 4 shows that there is a marked improvement in the shear map estimates for horizontal F factor. Therefore, using the shear map and correcting for altitude seems to provide an acceptable estimation of the horizontal F factor.

6. COMPARISON OF AIRCRAFT AND RADAR ESTIMATES OF VERTICAL F FACTOR

From formula (1), the vertical term of the F factor is estimated using the following formula (Again: K' is equal to one because the shear map is a one kilometer shear):

$$F_V = \frac{\Delta V}{\Delta R}\left(\frac{2h}{GS}\right) \qquad (3)$$

Figure 5 shows the shear map estimated vertical term versus the *in situ* F factor. A probable explanation for the poor performance of the downdraft estimates is the simplistic assumption used to estimate the downdraft velocity. Observations have shown that the downdraft velocity varies with altitude as well as across the radius of a microburst. A better estimation of the vertical F factor needs to be developed that is capable of incorporating the aircraft's location within the microburst.

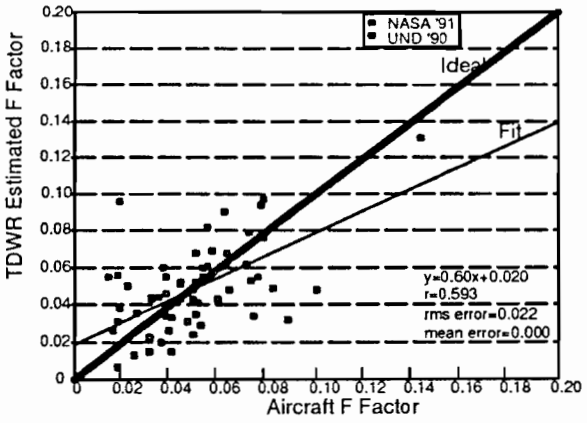

Figure 4. TDWR shear map vs. aircraft horizontal F factor at F total peak time using altitude profile correction.

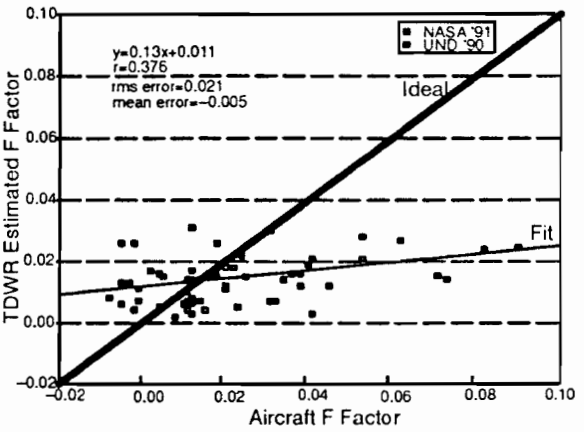

Figure 5. TDWR shear map vs. aircraft vertical F factor at F total peak time.

7. CONCLUSION

While the current TDWR microburst algorithm performs extremely well in detecting microburst hazards, some enhancements are needed to improve its ability to characterize the hazard in terms of the F factor. It has been shown that the current microburst shapes overestimate the F factor hazard if the aircraft does not encounter the core of the microburst. A shear–based approach was developed which allows the horizontal F factor to be estimated accurately. However, the vertical F factor term remains poorly estimated due to an overly simplistic mass continuity assumption.

In order to improve the estimate of the vertical F factor, future research will focus on fitting an analytical microburst model to shear–based microburst detections. Such a shear–based algorithm is currently under development as part of the Integrated Terminal Weather System (ITWS) program (Dasey, 1992). This new algorithm will allow the microburst hazard to be more accurately characterized by providing better localization of regions of intense horizontal shear and a better estimation of downdraft intensity.

8. REFERENCES

Bowles, R. L, 1990: "Reducing Windshear Risk Through Airborne Systems Technology", 17th Congress on the Aeronautical Sciences, Stockholm, Sweden, Sep. 9–14, 1990.

Britt, C.L. and Bracalente, E, 1992: "NASA Airborne Radar Windshear Detection Hazard Algorithm and the Detection of Wet Microbursts in the Vicinity of Orlando Florida," *Airborne Wind Shear Detection and Warning Systems,* Fourth Combined Manufacturers' and Technologists' Conference, Williamsburg, Virginia, (April 1992).

Dasey, T.J, 1993: "A Shear Based Microburst Detection Algorithm for the Integrated Terminal Weather System (ITWS)", 26th International Conference on Radar Meteorology, Norman, Oklahoma, May 24–28, 1993.

Oseguera, Rosa M. and Bowles, Roland L, 1988: "A Simple, Analytic 3–Dimensional Downburst Model Based on Boundary Layer Stagnation Flow," NASA TM–1000632, (July 1988).

Vicroy, Dan D, 1991: "A Simple, Analytical, Axisymmetric Microburst Model for Downdraft Estimation," NASA TM–104053, (February 1991).

COHERENT PROCESSING ACROSS MULTI–PRI WAVEFORMS

Mark E. Weber and Edward S. Chornoboy

MIT/Lincoln Lab
Lexington, Massachusetts

1. INTRODUCTION

Meteorological Doppler radars have typically utilized constant pulse–repetition intervals (PRI) to facilitate clutter filtering and estimation of weather echo spectral moments via pulse–pair or periodogram–based algorithms. Utilization of variable PRIs to support resolution of velocity ambiguities has been discussed, for example by Banjanin and Zrnic [1], but not implemented owing to difficulties associated with clutter filter design. Recent work by Chornoboy [2] presents design algorithms for time–varying finite impulse response (FIR) filters that achieve Chebyshev or mean–squared error (MSE) optimality when processing multi–PRI waveforms. This paper is a follow–on to that work, treating techniques for post–clutter filter processing (e.g. periodogram estimation) that are appropriate for such waveforms.

Our approach involves a least–squares fitting of the signal — sampled at a nonuniform rate — to a weighted sum of uniformly spaced sinusoids. The sinusoids or "basis functions" are chosen to span a Nyquist interval consistent with the longest PRI in the transmitted waveform, and need not be centered at zero Doppler. Determination of the sinusoid weightings — effectively a discrete Fourier transformation (DFT) — and the associated residual between the harmonic fit and the data are accomplished via multiplications of the signal vector with pre–computed matrices. The resulting spectrum estimate can be used directly for weather echo moment calculations, or can be inverse–Fourier transformed using conventional techniques to generate a time–domain signal representation.

This work has been motivated by a specific application — estimation of weather spectrum moments for a Wind Shear Processor (WSP) modification to the Federal Aviation Administration's Airport Surveillance Radar (ASR–9) [3]. Our approach supports candidate low–altitude radial wind estimation algorithms [3]–[6] that operate on frequency–domain signal representations and require that the radar's block–stagger PRI and the possibility of velocity ambiguities be accounted for in generating the spectrum estimates. In principle, however, these processing techniques are also applicable to weather radar systems such as WSR–88D and Terminal Doppler Weather Radar (TDWR) where range and Doppler ambiguities are an operational concern.

2. LEAST SQUARES HARMONIC FITTING

Data samples at arbitrary times t(n),

$$x_n = x[t(n)] \qquad n = 0,N-1 \qquad (1)$$

are modeled as the weighted sum of M harmonically related sinusoids:

$$\hat{x}_n = \sum_{m=0}^{m=M-1} y_m \exp[i2\pi(f_o+m\Delta f)t(n)] \quad . \quad (2)$$

Weights y_m are chosen so as to minimize the residual between the harmonic fit and the data samples:

$$\varepsilon^2 = \sum_{n=0}^{n=N-1} | x_n - \hat{x}_n |^2 \quad . \quad (3)$$

The solution and corresponding residual are:

$$\bar{y} = \bar{A}\,\bar{x} \qquad (4)$$
$$\varepsilon^2 = \bar{x}^H \bar{B}\,\bar{x} \quad .$$

Here $\bar{y}$ is the M–length column vector of harmonic weights y_m and $\bar{x}$ is the N–length column vector of data samples. The MxN matrix $\bar{A}$ and the NxN matrix $\bar{B}$ are given by

$$\bar{A} = -(\bar{\Phi}^H\bar{\Phi})^{-1}\bar{\Phi}^H \qquad (5)$$
$$\bar{B} = \bar{I} - \bar{\Phi}\bar{A} \quad .$$

where basis function elements

$$\phi_{n,m} = \exp[\, i2\pi(f_o+m\Delta f)t(n)] \qquad (6)$$

define the NxM matrix Φ.

The following considerations establish the number, M, and spacing, Δf, of sinsuoids used to model the signal. First, the number of sinusoids must be less than or equal to the number of data samples so that the system of equations (2) is not underdetermined:

$$M \leq N \quad . \quad (7)$$

Second, the transform of the frequency sampling "comb" (a comb in the time domain with spacing $1/\Delta f$) must not fold the signal over on itself:

$$\Delta f \leq [t(N)-t(0)]^{-1} \quad . \quad (8)$$

Finally, the maximum signal bandwidth representable by the sinusoid set must be consistent with the longest PRI in the transmitted waveform:

$$M\Delta f \leq [\max\{t(n)-t(n-1)\}]^{-1} \quad . \quad (9)$$

We choose Δf so as to satisfy the equality in equation (8), then

The work described has been sponsored by the Federal Aviation Administration. The U.S. Government assumes no liability for its contents or use thereof.

set M to be the largest integer that satisfies equation (9). This guarantees that condition (7) is satisfied.

3. APPLICATION TO ASR–9 WSP

The ASR–9 utilizes a variable PRI to mitigate "blind" speeds for aircraft targets. During the period in which the antenna scans one beamwidth in azimuth, a block of eight pulses is transmitted at a long PRI, followed by ten pulses at a short PRI. Because the antenna rotation rate of the ASR–9 varies under wind loading, "fill pulses" at the long PRI may be inserted following the two pulse blocks in to maintain scan–to–scan azimuth registration of the waveform. The ratio of the long and short PRIs is 9:7 with a typical value for the long PRI of 1 ms. The associated Nyquist interval for the S–band radar is 53 m/s.

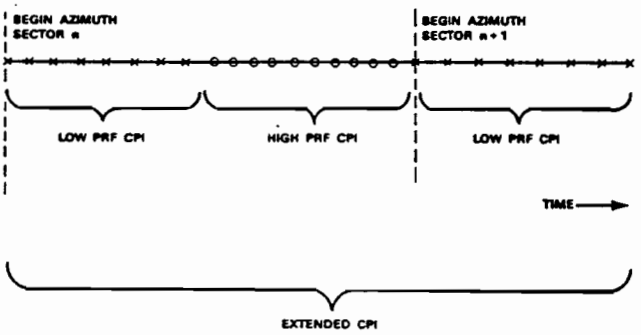

Figure 1. ASR–9 transmitted waveform.

In order to obtain a sufficient number of samples for clutter suppression and Doppler velocity estimation, the WSP operates coherently across three of the individual pulse blocks as shown. This "extended" coherent processing interval (CPI) spans 27 successive pulses and is the longest deterministic waveform available, owing to lack of *a priori* knowledge as to how many fill pulses will be inserted.

Figure 2 illustrates a candidate signal processing sequence used by the WSP to generate weather moment estimates. In-phase and quadrature signals are high–pass filtered using the shift–variant FIR designs described in [7]. Group delay is chosen so that the filter output sample spacing is equal to that of the input. Two samples at each end of the output data vector are discarded to minimize filter degradation at the beginning and end of the sequence. A first estimate of unambigous mean Doppler velocity is obtained through application of the "Chinese Remainder Theorem" to pulse–pair Doppler estimates obtained individually from the long– and short–PRI data blocks.

With a post–clutter filter data vector of length N=23, the conditions of equations (7) through (9) establish M=21 and $\Delta f = 48\ s^{-1}$ (2.5 m/s). Based on the Chinese Remainder Theorem estimate of unambiguous mean Doppler, one of two matrices $\overline{A}$, corresponding to basis functions with center frequency offsets f_o of respectively plus and minus 0.3 times the long–PRI Nyquist interval, is selected. Additional tests, described below, may be used to confirm that the selected basis function center frequency offset is appropriate. A "windowed" version (see below) of the matrix $\overline{A}$ is used to generate a spectrum estimate from the full 23–sample output of the clutter filter. Weather moment estimates, such as "low altitude" Doppler velocity [3]–[6], are generated from this full–resolution spectrum estimate.

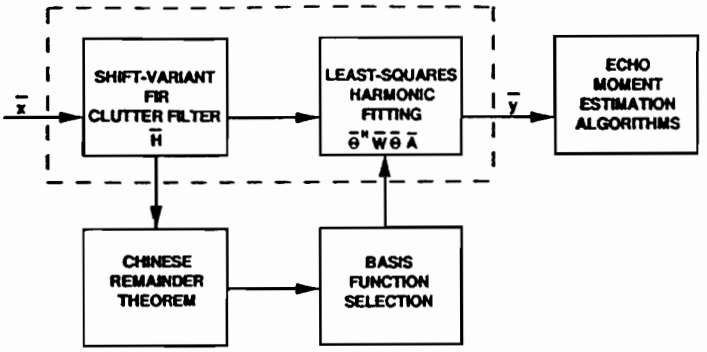

Figure 2. Block diagram of candidate signal processing sequence exploiting non–uniform PRI waveform for velocity ambiguity removal.

With this procedure, unaliased power spectrum estimates are obtained for weather signals between 0.8 and –0.8 times the long–PRI Nyquist interval. The resulting extended Nyquist interval (+/– 42 m/s) is sufficient for any weather conditions where aircraft landings or takeoffs would be attempted.

In the ASR–9 WSP application, resolution cells are revisited once every 5 seconds. Since weather parameters do not evolve this rapidly, the velocity ambiguity processing need not be repeated on every scan of the antenna (once per minute is sufficient). As shown by the dashed lines in Figure 2, on the remaining scans the matrix $\overline{A}$ can be preselected and cascaded with the matrix $\overline{H}$ that implements the shift–variant FIR filter.

Utilization of a matrix multiply to accomplish the signal processing leads to considerable flexibility. For example, clutter filtering, time–series data "windowing" and time–to–frequency transformation can be achieved through a single matrix multiply operation:

$$\overline{y} = \overline{\Theta}^H \overline{W}\, \overline{\Theta}\, \overline{A}\, \overline{H}\, \overline{x} \qquad . \quad (10)$$

Here, the elements of $\overline{\Theta}$ are those of a conventional inverse DFT, and $\overline{W}$ is a square "windowing" matrix whose non–diagonal elements are zero, and whose diagonal elements are the desired window function. If zero–padding to obtain finer velocity spacing of spectrum estimates is desired, zeroes are appended to the columns of $\overline{\Theta}$ and the rows and columns of $\overline{W}$, and $\overline{\Theta}^H$ is replaced by a square DFT matrix of appropriate order.

4. ILLUSTRATION OF MULTI–PRI PROCESSING

Figure 3 shows spectrum estimates for a sinsuoid of frequency 0.65 times the long–PRI Nyquist interval; the sinusoid has been sampled at 27 points corresponding to the ASR–9 waveform illustrated in Figure 1. The left and right panels are estimates generated using equation (10) with the above basis function offsets f_o of respectively minus and plus 0.3. The filter matrix $\overline{H}$ has been chosen to be all–pass in this example. The correct choice of basis function results in a spectrum with its peak correctly positioned and Doppler sidelobes that are consistent with theoretical performance of the Blackman taper used to construct the window matrix. Incorrect choice of f_o re-

sults in signficant whitening of the signal spectrum and an order of magnitude increase in the residual ε^2.

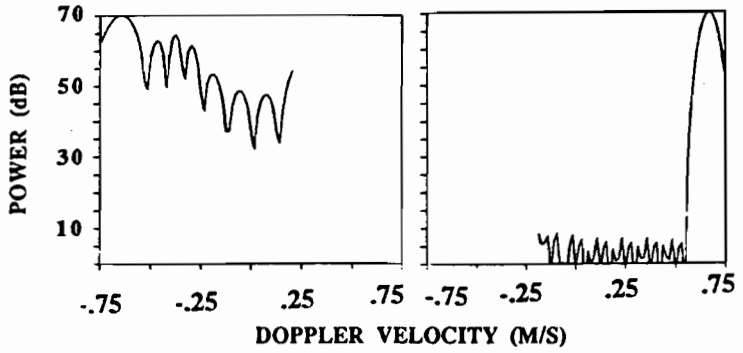

Figure 3. Spectrum estimates from equation (10) applied to simulated sinusoid sampled at non–equal intervals. Sinusoid normalized frequency is 0.65 and basis function offsets are –0.3 (left) and 0.3 (right).

Criteria testing the appropriateness of the choice of basis function frequency offset f_o can be used to reduce the likelihood of a gross unfolding error from the initial Chinese Remainder theorem Doppler estimate. As illustrated above, examples of such criteria are the magnitudes of the harmonic model residuals ε^2 and the "whiteness" (power ratio of minimum to maximum spectrum component) of the spectra estimated using different choices for f_o. Experiments using simulated weather signals with varying signal to noise, signal to clutter and spectrum widths have indicated that the "whiteness" test is generally more robuste.

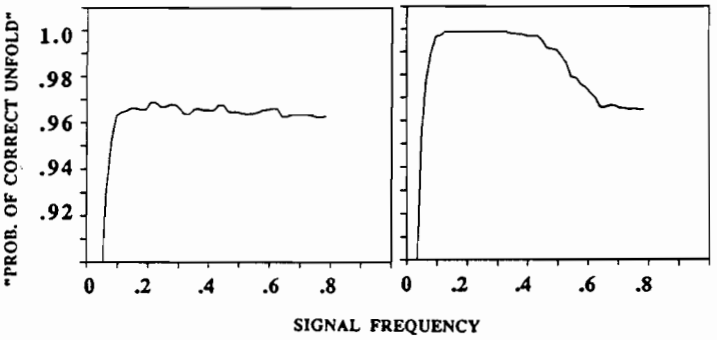

Figure 4. "Probability of correct unfold" as described in the text versus signal mean Doppler. The left panel treats the initial Chinese remainder theorem estimate. In the right panel, the "whiteness" test is used to affirm that this initial choice is appropriate

Figure 4 illustrates the concept. Monte Carlo simulations were run using a weather signal of moderate spectrum width (5 m/s) and low signal–to–noise ratio (5 dB) whose normalized mean Doppler frequency was varied from 0 to +0.8. The figure plots the probability that the positive basis function frequency offset is correctly selected. (Note that for signals with mean Doppler less than 0.2 minus the signal bandwidth, either choice for f_o is appropropriate). Our initial estimate (solid curve in the left panel) sets the sign of the selected basis function frequency offset equal to that of the Chinese Remainder theorem Doppler estimate and, in this example, is incorrect about 3.5% of the time. This estimate is checked against the choice for f_o that minimizes the "whiteness" of the resulting spectrum. The "whiteness" test complements the initial estimate by providing near perfect selection of basis function frequency offset as long as signal Doppler is not so high that significant power is outside the shifted Nyquist interval. When both tests are applied (right panel) the probability of selecting the appropriate sign of f_o, or flagging the data as suspect owing to disagreement, is near unity out to a normalized signal frequency of 0.5. At higher signal Doppler, the frequency offest selection accuracy degrades to the "baseline" value associated with the Chinese Remainder theorem. This degradation at high Doppler magnitude could be eliminated by testing of additional basis functions with larger frequency offsets (e.g. ± 0.9).

5. OTHER APPLICATIONS

Base data degradation produced by range and Doppler ambiguities remain a fundamental problem for weather radar, particularly with systems such as WSR–88D and TDWR where automated meteorological detection algorithms are used. The NEXRAD Technical Advisory committee recently identified range/Doppler ambiguities as the second highest priority unmet technical need (after data archiving). Initial Operational Test and Evaluation (OT&E) of the TDWR in Oklahoma City has likewise illustrated that second trip weather contamination and/or incorrectly dealiased radial velocity estimates may degrade the operational capabilities of the radar.

The work described here and in references [2] and [7] point the way to processing techniques that could ameliorate these problems when coupled with signal waveform changes. Reliable resolution of Doppler ambiguities would allow for operation at a lower average pulse repetition frequency, which in turn, would reduce the impact of range folding. While the signal processing requirements are considerable (approximately 200 MFLOPS in our ASR–9 application), rapid evolution in digital processing hardware capability makes such approaches feasible. We note, for example, that commercially available single–board array processing cards achieving this throughput are available for under $20,000.

REFERENCES

1. Z. Benjamin and D. Zmic, Clutter rejection for Doppler weather radars which use staggered pulses. IEEE Transactions on Geoscience and Remote Sensing, 29, 610–620, 1991.

2. E. Chornoboy, Clutter filter design for multiple–PRT signals, Preprint Volume: 26th International Conference on Radar Meteorology, Norman, OK, May 24–28, 1993, AMS.

3. M. Weber, M. Stone, C. Primeggia, J. Anderson, Airport Surveillance Radar based wind shear detection, Preprint Volume: 4th International Conference on the Aviation Weather System, Paris, France, June 24–28, 1991, AMS.

4. D. Atlas, The detection of low level windshear with Airport Surveillance radar, 3rd International Conference on the Aviation Weather System, Anaheim, Ca., Jan 30 – Feb 3, 1989, AMS.

5. J. Anderson, Techniques for the detection of microburst outflows using Airport Surveillance Radars, 3rd International Conference on the Aviation Weather System, Anaheim, Ca., Jan 30 – Feb 3, 1989, AMS.

6. E. Chornoboy, Optimal mean velocity estimation for Doppler weather radars, IEEE Transactions on Geoscience and Remote Sensing, 32, 1993 (in press).

7. E Chornoboy, Addendum to "Ground Clutter Processing for Wind Measurements with Airport Surveillance Radars": Optimum Time–Varying Designs, Lincoln Laboratory Report ATC–191, 1993 (in press).

CLUTTER FILTER DESIGN FOR MULTIPLE-PRT SIGNALS [1]

Edward S. Chornoboy

MIT Lincoln Laboratory
Lexington, Massachusetts 02173

1 INTRODUCTION

The trade-off of range vs. velocity ambiguity is fundamental and operationally significant for many S- and C-band pulsed Doppler weather radars. Transmission schemes using multiple pulse repetition times (PRTs) [i.e., nonuniform pulse spacing] offer the potential for extending the unambiguous measurement range by resolving intervals of velocity ambiguity. Unfortunately, multiple PRT methods can be problematic with low-elevation scanning when ground clutter removal is required. We have constructed both Chebyshev and mean-squared error (MSE) design algorithms (Chornoboy, 1993) that deal with design in the complex domain; the MSE algorithms are described below.

2 DESIGN ISSUES

Consider the design of a finite impulse response filter. For an N-coefficient filter, as many as K designs may be required, where K is the number of distinct pulse arrangements of length N. Since it is easier to consider a specific example, we focus primarily on the simple case shown in Fig. 1, that of an alternating-PRT scheme. Here two filters are "multiplexed" in the sense that one set of coefficients[2] $H_1 = [h_{10} \cdots h_{1\,N-1}]^T$ operates on sequences beginning with the longer pulse interval T_1, and a second set (H_2) operates on sequences beginning with T_2.

Velocity estimates for the alternating-PRT signal of Fig. 1 can be obtained by using the single-lag autocorrelation method known as Pulse Pair. If $\hat{R}_1 = \hat{R}(T_1)$ represents an autocorrelation estimate obtained from pulses separated by T_1, then the Doppler velocity (shift) can be estimated as $\hat{V}_1 = -(\lambda/4\pi T_1)\arg(\hat{R}_1)$, where λ is the radar wavelength. Similarly, estimates $\hat{R}_2$ and $\hat{V}_2$ can be obtained corresponding to the interval T_2.

The estimates $\hat{V}_1$ and $\hat{V}_2$ "fold" at values of V determined by the intervals T_1 and T_2. If $T_1 \neq T_2$, velocity folding can be detected and corrected by examining the phase difference between $\hat{R}_1$ and $\hat{R}_2$. This can either be done using the "difference" $\arg(\hat{R}_1\hat{R}_2^*)$, as discussed by Zrnić and Mahapatra (1985), or the difference $\hat{V}_1 - \hat{V}_2$, as considered by Sirmans et al. (1976). The latter is illustrated in Fig. 2, which plots ideal relationships for the case $2T_1 = 3T_2$. The upper plot shows the folding patterns for $\hat{V}_1$ and $\hat{V}_2$ as functions of true velocity. The lower plot illustrates the behavior of the difference $\Delta V = \hat{V}_1 - \hat{V}_2$, and to the extent that this quantity has a unique mapping to intervals of true velocity, ambiguities can be resolved.

It is desirable to have a magnitude response over the extended velocity interval that is free of "blind speeds" so that measurements $\hat{V}_1$ and $\hat{V}_2$ will always be available. However, because $\hat{R}$ phase is key to velocity estimation and ambiguity resolution, it too is an important aspect of the filter design process. Figure 3 shows a staggered-

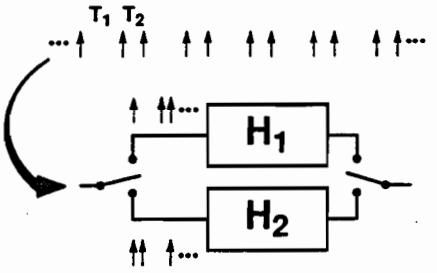

Figure 1: Alternating-PRT Filtering Scheme.

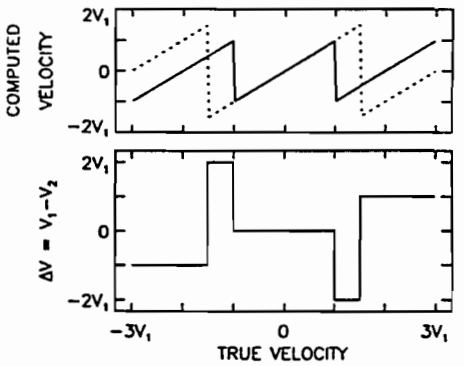

Figure 2: Ideal Dealiasing Using ΔV Method.

[1] The work described has been sponsored by the Federal Aviation Administration. The U.S. Government assumes no liability for its contents or use thereof.

[2] Throughout, superscript "T" is used to represent matrix transpose; "$*$", complex conjugate; and "$\dagger$", conjugate transpose.

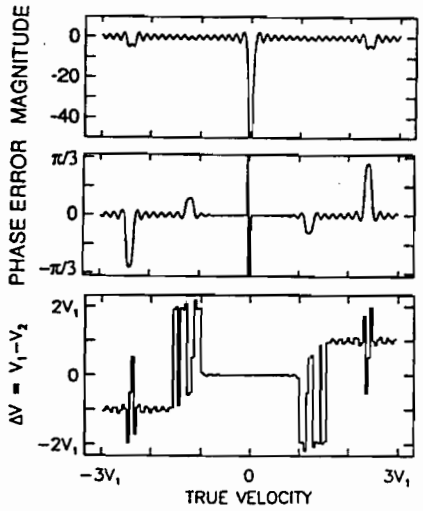

Figure 3: Filter Response and ΔV Transfer Function for Staggered Design Without Phase Control.

PRT design similar to that achievable by adapting uniform sampling methods [Banjanin and Zrnić (1991)]. For an assumed 3:2 stagger spacing, a 33-coefficient filter was designed to provide a stopband half width equaling 0.04 V_1. Although a near "flat" magnitude response has been obtained (top), there are intervals where the phase response deviates significantly from linear phase (middle), and the effect of this phase error on the ideal ΔV transfer function (bottom) is near devastating. Banjanin and Zrnić (1991) have described a method that would work around those areas where the ΔV measure is most impaired.

3 MSE DESIGN EQUATIONS

The frequency response of filter H_k is defined by

$$\mathcal{H}_k = \mathcal{H}_k(\omega) \stackrel{\text{def}}{=} \sum_{n=0}^{N-1} h_{kn}\, e^{\,j\omega\tau_n}\,, \qquad (1)$$

where τ_n is the time of the n^{th} input sample (relative to the filter start). Let $\mathcal{D}_k = \mathcal{D}_k(\omega)$ represent the desired output response. The filter design problem is to find coefficients H_k that best fit functions $e^{\,j\omega\tau_n}$ to the desired frequency response $\mathcal{D}_k$.

It is straightforward to set up MSE design functionals by taking M discrete frequency samples of $\mathcal{H}_k$ and $\mathcal{D}_k$. First, define $M \times N$ real-valued matrices C and S, where C is given by

$$C = \begin{bmatrix} \cos\omega_0\tau_0 & \cdots & \cos\omega_0\tau_{N-1} \\ \vdots & & \vdots \\ \cos\omega_{M-1}\tau_0 & \cdots & \cos\omega_{M-1}\tau_{N-1} \end{bmatrix}, \qquad (2)$$

and S is defined similarly using "sin" instead of "cos". Second, let σ_k represent the desired output-sample times (i.e., group delay) for the filters, and construct output vectors $\tilde{C}_k$ and $\tilde{S}_k$, where $\tilde{C}_k = [\cos\omega_0\sigma_k \cdots \cos\omega_{M-1}\sigma_k]^T$, etc. Finally, group "sin" and "cos" terms together to form complex input $\Psi = C + jS$ and output $\tilde{\Psi}_k = \tilde{C}_k + j\tilde{S}_k$, and specify the desired magnitude response via an $M \times M$ diagonal matrix D. The ideal output response for filter k is $D\tilde{\Psi}_k$; the approximation to this is ΨH_k, and the approximation error is $\mathcal{E} = \Psi H_k - D\tilde{\Psi}_k$. The weighted squared error $\mathcal{E}^\dagger Q \mathcal{E}$ can be minimized to obtain an MSE solution for H_k. The $M \times M$ real-valued matrix Q is used to introduce relative weighting for pass-, transition-, and stop-band regions. We have found it useful also to place a constraint on the maximum gain of the filter, which can be included via a term such as $H_k^T H_k$.

Although the above provides a design based on minimizing the complex-domain error, it may not be sufficient because it does not permit independent control of phase vs. magnitude error. Let $\epsilon_k = \epsilon_k(\omega) = \omega\sigma_k - \angle\mathcal{H}_k$ represent the phase error for filter k. For $|\epsilon_k| < \pi/2$, the trigonometric inequality

$$|\epsilon_k| \le \frac{\pi}{2}\,|\sin(\omega\sigma_k - \angle\mathcal{H}_k)| \qquad (3)$$

holds, and where $|\mathcal{H}_k| \neq 0$,

$$\sin\angle\mathcal{H}_k = \frac{1}{|\mathcal{H}_k|}\sum_n h_{kn}\sin\omega\tau_n\,. \qquad (4)$$

Equations 3 and 4 can be combined to yield the phase-error constraint

$$|\epsilon_k| \le \frac{\pi}{2\,|\mathcal{H}_k|}\left|\sum_n h_{kn}\sin\omega(\sigma_k - \tau_n)\right|\,, \qquad (5)$$

which can be used to force $|\epsilon_k|$ small, to the extent that $|\mathcal{H}_k|$ cooperates. Define the $M \times N$ matrix $\Theta_k =$

$$\begin{bmatrix} \sin\omega_0(\sigma_k - \tau_0) & \cdots & \sin\omega_0(\sigma_k - \tau_{N-1}) \\ \vdots & & \vdots \\ \sin\omega_{M-1}(\sigma_k - \tau_0) & \cdots & \sin\omega_{M-1}(\sigma_k - \tau_{N-1}) \end{bmatrix},$$

and form squared error term $\Phi_k^T P \Phi_k$, where $\Phi_k = \Theta_k H_k$ and P is an optional weighting matrix for the phase error.

An error functional for the phase-controlled design can be written

$$f(H_k) = \mathcal{E}^\dagger Q \mathcal{E} + \Phi_k^T P \Phi_k + H_k^T H_k\,. \qquad (6)$$

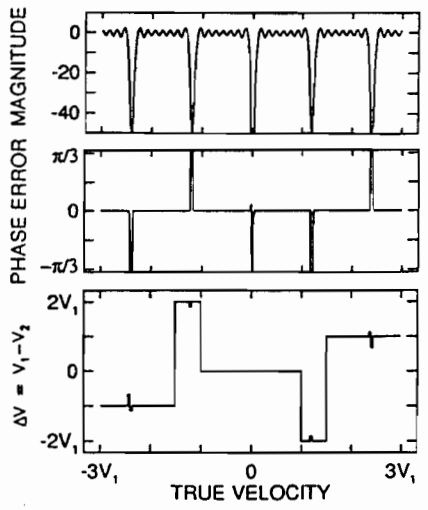

Figure 4: Filter Response and ΔV Transfer Function for Staggered Design With Excessive Phase Control.

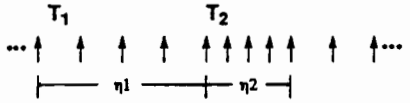

Figure 5: A Block-Staggered Sampling Scheme

This is quadratic in H_k and has solution

$$H_k = [\Re e(\Psi^\dagger Q \Psi) + \Theta_k^T P \Theta_k + I]^{-1} [\Re e(\Psi^\dagger Q D \tilde{\Psi}_k)]$$
$$= [C^T Q C + S^T Q S + \Theta_k^T P \Theta_k + I]^{-1} \cdot [C^T Q D \tilde{C}_k + S^T Q D \tilde{S}_k]. \quad (7)$$

Note that this solution only requires real-domain computation.

At the extreme $P = \emptyset$ (i.e., no phase control), the design of Fig. 3 results. If P is instead set very large, placing high priority on a linear phase response, the design of Fig. 4 results. This second design approaches the "split uniform PRT" filter discussed by Banjanin and Zrnić (1991). Linear phase is obtained at the expense of introducing notches (blind speeds) in the magnitude response. For the alternating-PRT signal, magnitude response blind/dim speeds vs. nonlinear phase is a fundamental trade-off which no optimal design can fully overcome.

An additional "design" option exists however for weather-radar application because coherent averaging over many intervals T_1 (T_2) is typically employed. A simple extension to the design illustrates one practical potential. Consider the block-staggered signal structure illustrated in Fig. 5. Pulse spacing T_1 is repeated η_1 times, followed by interval T_2 η_2 times; after which the pattern repeats. This signal requires $K = \eta_1 + \eta_2$ filter coefficient sets. As with the above alternating-PRT example, it is unlikely that exact linear phase can be achieved without some compromise in magnitude response. However, the added complexity of the pulse pattern enables an improved balance between magnitude and phase response. Furthermore, since there is variety in the filters affecting T_1 (T_2) intervals (across the confines of one block), phase and magnitude responses can be balanced among filters by "dithering" (distributing) the error. Very satisfactory response profiles can result as shown in Fig. 6, which shows the results for a (4,4) block-stagger design using a phase-control weighting intermediate to that used in Figs. 3 and 4.

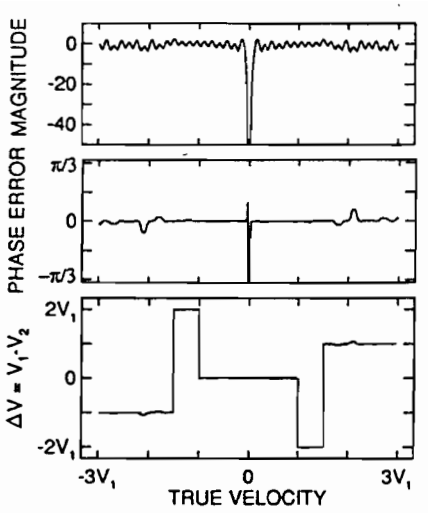

Figure 6: Filter Response and ΔV Transfer Function for Block-Staggered Design With Phase Control.

References

[1] Z. Banjanin and D. Zrnić. Clutter rejection for Doppler weather radars which use staggered pulses. *IEEE Transactions on Geoscience and Remote Sensing*, 29(4):610–620, 1991.

[2] E. Chornoboy. FIR design methods for non-uniformly sampled signals. Technical Report 976, MIT Lincoln Laboratory, Lexington, Massachusetts, 1993.

[3] D. Sirmans, D. Zrnić, and B. Bumgarner. Extension of maximum unambiguous Doppler velocity by use of two sampling rates. In *Proceedings; 17th Conference on Radar Meteorology*, pages 23–28, 1976.

[4] D. Zrnić and P. Mahapatra. Two methods of ambiguity resolution in pulse Doppler weather radars. *IEEE Transactions on Aerospace and Electronic Systems*, AES-21(4):470–483, 1985.

ANOMALOUS PROPAGATION ASSOCIATED WITH THUNDERSTORM OUTFLOWS

Mark E. Weber, Melvin L. Stone and Joseph A. Cullen
MIT/Lincoln Lab Lexington, Massachusetts

1. INTRODUCTION

Battan [1] noted that ducting of radar energy by anomalous atmospheric refractive index profiles and resulting abnormally strong ground clutter can occur during three types of meteorological circumstance: (i) large scale boundary layer temperature inversions and associated sharp decrease in moisture with height — these are often created by nocturnal radiative cooling; (ii) warm, dry air moving over cooler bodies of water, resulting in cooling and moistening of air in the lowest levels; (iii) cool, moist outflows from thunderclouds.

In contrast to the first two types of anomalous propagation (AP), radar ducting associated with thunderstorm outflows is quite dynamic and may mimic echoes from precipitating clouds in terms of spatial scale and temporal evolution. While non–coherent weather radars (e.g. WSR–57) are obviously susceptible to false storm indications from this phenomenon, Doppler radars that select the level of ground clutter suppression based on "clear day maps" may also fail to suppress the AP–induced ground clutter echoes. Operational Doppler radar systems known to be susceptible to this phenomena are the National Weather Service's WSR–88D (Sirmans, personal communication) and the Federal Aviation Administration's Airport Surveillance Radar (ASR–9) six–level weather channel [2].

In this paper, characteristics of thunderstorm outflow–generated AP are documented using data from a testbed ASR–9 operated at Orlando, Florida. The testbed radar's rapid temporal update (4.8 seconds per PPI scan) and accurate scan–to–scan registration of radar resolution cells enabled characterization of the spatial and temporal evolution of the AP–induced clutter echoes. We discuss implications of these phenomenological characteristics on operational systems, specifically the ASR–9. Algorithms for discrimination between true precipitation echoes and AP–induced ground clutter are discussed.

2. AP MEASUREMENTS WITH ASR–9

The ASR–9 testbed in Orlando, Florida [3] operated at 2.8 GHz, transmitting a 1 MW, 1 μs uncoded pulse at an average PRF of 1100 per second. The antenna's half–power beamwidth is 1.4° in azimuth and approximately 5° in elevation; the tilt of the antenna places the peak of the elevation pattern 2° above the horizon and the lower half–power point on the horizon. In-phase and quadrature signals are sampled at intervals of 0.775 μs and simultaneously stored on high density instrumentation tape and processed to generate real–time displays of precipitation reflectivity, mean Doppler and spectrum width. Small–scale divergent outflows (microbursts) and outflow boundaries (gust fronts) are detected by automated algorithms, displayed and tracked in real time. The instrumented range for the algorithms extends 30 km from the radar; maps of weather spectrum moments are generated to a range of 111 km.

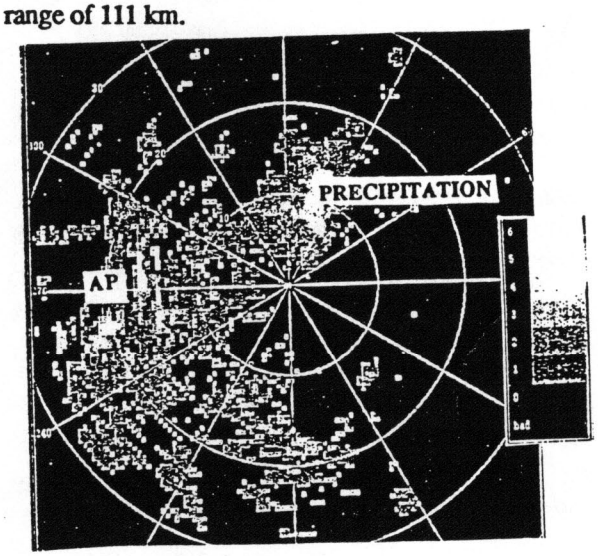

Figure 1. PPI scan of reflectivity (quantized in NWS "VIP" units) during an AP–episode. Range rings at 10 km intervals.

Data from six separate occurrences of thunderstorm–generated AP during the months of August and September 1991 and 1992 were examined for this paper. Significant enhancement of ground clutter during these episodes was observed at ranges up to 50 nmi — the strongest returns exceeded 65 dBz equivalent reflectivity factor and the largest AP area observed was about 200 square kilometers. Duration of the significant AP–induced ground clutter episodes varied from 1.25 to more than 2.5 hours. During these episodes, individual "patches" — closed regions containing echoes in excess of 35 dBz equivalent reflectivity — varied in duration from a few minutes to the lifespan of

The work described has been sponsored by the Federal Aviation Administration. The U.S. Government assumes no liability for its contents or use thereof.

the AP episode. Figure 1 shows a reflectivity map generated by the ASR–9 testbed during one of these episodes. Normal ground clutter has been removed by highpass filters, selected using a "clear day map" [4]; the remaining echoes are precipitation and AP–induced ground clutter ; the latter echoes are primarily to the south and west of the radar at ranges greater than 15 km. Note that some of the AP echoes to the west are contiguous to or even embedded in 20 to 35 dBz precipitation echoes to the west of the radar.

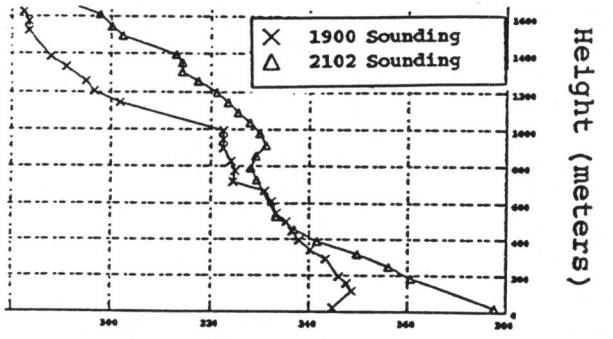

Figure 2. Radar refractivity ("N units") profile derived from pre–and post–gust front rawindsonde soundings.

Each AP episode occurred following the passage of a thunderstorm outflow boundary (gust front) over the radar site. In the above example, a strong, eastward–moving gust front passed over the ASR–9 about 30 minutes prior to the depicted scan. Pre– and post–gust front rawindsonde soundings showed significant cooling and moistening in the lowest 500 meters; maximum changes in temperature and dew point were at the surface and equalled 6 and 3 °C respectively. The resulting increase in radio refractivity gradient below 500 m is shown in Figure 2. The AP areas are observed only in the sector behind the gust front, implying that the superrefractive environment must be maintained along the entire path between the radar and the ground scatterers responsible for the echoes.

In general, the patches of strong AP–induced ground clutter appear suddenly (when the outflow boundary has passed 5–10 km beyond the radar), remain approximately constant in intensity and spatial extent for a period of time, then dissipate rapidly over the entire affected area. A characteristic time scale for onset or dissipation of individual AP patches is 5 to 10 minutes. During the constant phase of the AP episode, echo intensity variation in time is small, consistent with scan–to–scan fluctuations in normal ground clutter cross– section [4]. Specific geographic areas are consistent sources of strong echoes with repeatable spatial reflectivity patterns.

Figure 3 compares power spectrum estimates from AP–induced ground clutter breakthrough and stratiform precipitation. Spectra of the AP–induced echoes are indistinguishable from normal clutter, consisting of a zero mean Gaussian component with spectrum width (0.75 m/s) consistent with antenna scan modulation. Precipitation echoes as sensed by the fan–beam ASR–9 — even the low mean Doppler stratiform rain echo shown in Figure 3 — consistently exhibit significantly larger spectrum width owing to vertical shear in the horizontal wind.

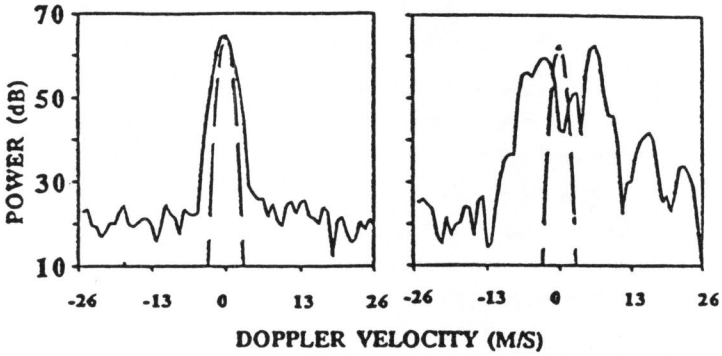

Figure 3. Power spectrum estimates of AP–induced clutter (left) and stratiform precipitation (right). Dashed lines show theoretical antenna scan–modulation spectrum.

3. AP–Induced Ground Clutter Rejection

Use of a high–pass ground clutter filter in all range–azimuth resolution cells would eliminate stationary clutter breakthrough caused by AP. Such filtering may not be desirable, however, since low–Doppler power removed by the filters may result in biases in weather reflectivity or mean Doppler estimates. This effect is exacerbated in the case of the rapid–scanning ASR–9, since the available coherent processing intervals are short (8 or 10 pulses) and the transition bands associated with achievable high–pass filters are large [4].

The ASR–9 weather channel and the WSR–88D attempt to minimize these biases by utilizing site–specific clear day maps of normal ground clutter to select the minimum level of clutter suppression necessary to achieve acceptable weather signal to clutter ratios. With this scheme, a "censoring" function should be introduced to identify stationary ground clutter breakthrough caused by abnormal propagation conditions.

Data from affected resolution cells are flagged and can be either disregarded in subsequent processing, or reprocessed using a more attenuating high–pass filter so as to suppress the clutter component of the echo.

We have examined two algorithms for discriminating between AP ground clutter breakthrough and actual precipitation echoes; both depend on the differing spectral characteristics of AP and precipitation echoes. Direct calculations of echo spectrum moments were utilized by an ASR–9 Wind Shear Processor [3] to censor AP–induced clutter breakthrough. The censor flag was set for range–azimuth resolution cells where the mean Doppler velocity was less than 1 m/s and the echo spectrum width was less than 1.5 m/s. Spatial consensus filters were applied to the censor flags (e.g. M–of–N filters along the range axis or 2–dimensional median filters) to remove "speckle" associated with weather moment estimate errors, particularly in the lower intensity AP areas. Figure 4 illustrates the effect of this censoring process using the scan shown previously. The censoring process largely removes the AP without significant impact on the precipitation echoes. The capability to remove AP echoes from the ASR–9's six–level reflectivity display was favorably received by the Orlando Air Traffic Control team during operational testing of the Wind Shear Processor in 1991 and 1992.

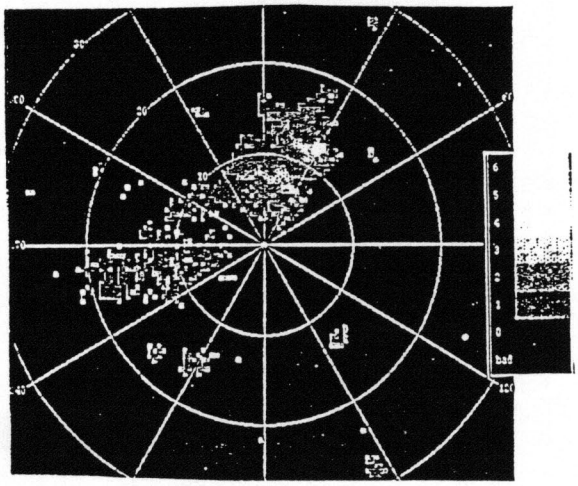

Figure 4. As in Figure 1 but with AP–discrimant enabled.

An alternate approach [2] exploits the "inverse matched filter" characteristics of the high–pass ground clutter filters. AP–induced clutter echoes will be subject to large attenuation when passed through these filters; attenuation of weather echoes with higher mean Doppler and spectrum width is much smaller. A power threshold test applied to the ratio of clutter filter input and output can effectively discriminate between AP–induced clutter breakthrough and precipitation. Details and performance examples are provided in [2].

The above techniques appear sufficient for Air Traffic Control applications where some errors in the exact intensity and areal extent of precipitation echoes are tolerable. Improved performance, useful for example in hydrological applications, may be obtainable by augmenting these single–gate spectral discriminants with "expert system" knowledge on the characteristics of AP–induced echoes and the likelihood of superrefraction. Elements of such a system would include measurements of the spatial statistics of the echoes, surface temperature and humidity measurements — potentially augmented by a refractometer, reliable automated detection of outflow boundaries [5] and knowledge of the locations of ground scatterers likely to be illuminated during AP. The site specific information necessary for this last element may be obtained by means of detailed terrain maps and appropriate propagation models, or experimentally through accumulation of statistics on scattering regions from many AP episodes.

4. Summary

Anomalous propagation, while well documented since early work on radar meteorology, remains an operational problem — particularly when it occurs in association with thunderstorm activity. This paper discussed spatial, temporal and spectral properties of AP–induced ground echoes associated with surface outflows from thunderclouds. We used data from a testbed ASR–9 to demonstrate a reliable spectral discriminant between AP–induced ground echoes and actual precipitation returns. In combination with additional sources of information relevant to the onset of AP, we believe that performance sufficient to support automated hydrological monitoring in the presence of this interferer can also be achieved.

REFERENCES

1. L. Battan, Radar Observations of the Atmosphere, University of Chicago Press, 1959.
2. D. Puzzo, S. Troxel, M. Meister, M. Weber, J. Pieronek, ASR–9 Weather Channel Test Report, Lincoln Laboratory Report ATC–165, DOT–FAA–PS–89–3, 1989.
3. M. Weber, M. Stone, C. Primeggia, J. Anderson, Aiport Surveillance Radar Based Wind Shear Detection, Preprint Volume: Fourth International Conference on Aviation Weather Systems, June 24–28, 1991, Paris, France, AMS.
4. M. Weber, Ground Clutter Processing for Wind Measurments with Airport Surveillance Radars, Lincoln Laboratory Report ATC–143, DOT–FAA–PM–87–21, 1987.
5. R. Delanoy and S. Troxel, A Machine Intelligent Gust Front Algorithm for Doppler Weather Radars, Preprint Volume: 26th International Conference on Radar Meteorology, 24–28 May, 1993, Norman, OK., AMS.

REAL–TIME MULTIPLE SINGLE DOPPLER ANALYSIS WITH NEXRAD DATA

F. Wesley Wilson, Jr. and Rodney E. Cole

MIT/Lincoln Laboratory
Lexington, Massachusetts

and

John A. McGinley and Steven C. Albers

NOAA/ERL/Forecast Systems Laboratory
Boulder, Colorado

1. INTRODUCTION

As part of the Aviation Weather Development Program of the Federal Aviation Administration, a high resolution winds analysis system was demonstrated at Orlando International Airport (MCO) in the summer of 1992. The purpose of this demonstration was to illustrate the winds analysis capability possible from operational sensors in the mid '90s. An important part of the design of this system was the development of a procedure for the assimilation of Doppler data from multiple radars. This procedure had to be able to automatically handle regions with missing data from one or more radars, as well as avoid baseline instability. The two operational radars scanning the analysis region were the National Weather Service WSR–88D (NEXRAD) radar located approximately 65 km east and slightly south of MCO, and the MIT prototype Terminal Doppler Weather Radar (TDWR) located 7 km due south of the airport. The base data from these two Doppler radars were the major information component for the analysis system.

Our system includes the most recent improvements in the winds analysis portion of the Local Analysis and Prediction System (LAPS) developed by the Forecast Systems Laboratory (McGinley *et al.*, 1991). LAPS is designed to run locally on systems affordable for operational weather offices and takes advantage of all sources of local data at the highest possible resolution. Our implementation for the airport terminal region is called the Terminal–area LAPS (T–LAPS). LAPS formerly had a technique for the assimilation of data from a single Doppler radar. We have modified that technique for the assimilation of data from the two available radars. Our approach, using a Multiple Single Doppler Analysis (MSDA) technique, is more suited for unsupervised operational analysis than traditional Dual Doppler Analysis (DDA), because it is able to handle such problems as incomplete data and baseline instability. We will describe the T–LAPS analysis, with particular attention to our implementation of MSDA, and give some examples from our demonstration.

*The work described here was sponsored by the Federal Aviation Administration. The United States Government assumes no liability for its content or use thereof.

2. LAPS WINDS ANALYSIS OVERVIEW

The LAPS winds analysis (Albers, 1992) uses a Barnes (1964) objective analysis scheme. The analysis acquires a background wind field and recent wind observations in the analysis region, and produces an analyzed wind field on a 3D grid. LAPS was designed to be computationally efficient and compatible with a background wind field provided by a previous analysis or numerical forecast model. For the demonstration only the horizontal winds were analyzed.

The steps in the analysis process are as follows:

1. For each observation, the difference between the u component of the observed wind and the u component of the background wind at the grid point nearest the observation is computed. Likewise, a difference is computed for the v component.
2. At each analysis point, weighted means of the u and v difference values are computed, to form a correction term which is an estimate of the vector difference between the actual wind and the background wind at that point. The weights depend on the horizontal and vertical distances from the observation location to the analysis point, a radius of influence that varies locally depending on the ambient data density, and sensor type.
3. The correction terms are added to the background wind to form the analyzed wind field.

Doppler radars measure the component of the wind only along the radar beam. Before the above process can be applied to Doppler radar data, the Doppler observations must be transformed into vector observations.

3. LAPS SINGLE DOPPLER ANALYSIS

This section details the process by which Doppler radar observations are brought into the LAPS analysis. The idea is to transform the single component observations from a Doppler radar into vector quantities, and then to use these vectors as additional observations.

The steps used to bring Doppler observations into the analysis are as follows:

1. An analyzed wind field is computed using the background wind field and the non–radar observations as discussed in

Section 2.
2. The wind field from Step 1 is adjusted at points with a Doppler wind speed estimate. At these points, the component of the wind along the radar beam is set to the Doppler value. The perpendicular component is unchanged.
3. The resulting wind vectors at points with a Doppler value are considered to be "radar vector observations".
4. The final analysis is computed from the original background wind field, the true vector observations, and the "radar vector observations" as described in Section 2.

4. MULTIPLE SINGLE DOPPLER ANALYSIS

The Multiple Single Doppler Analysis (MSDA) developed for T–LAPS is a simple extension of the standard LAPS Doppler analysis. The steps used to bring multiple Doppler observations into the analysis are as follows:
1. An analyzed wind field is computed using the background wind field and the non–radar observations as discussed in Section 2.
2. The wind field from Step 1 is adjusted at points with a NEXRAD Doppler wind speed estimate. At these points, the component of the wind along the radar beam is set to the Doppler value. The perpendicular component is unchanged.
3. The wind field from Step 2 is adjusted at points with a TDWR Doppler wind speed estimate. At these points, the component of the wind along the radar beam is set to the Doppler value. The perpendicular component is unchanged.
4. The resulting wind vectors at points with at least one Doppler value are considered to be "radar vector observations".
5. The final analysis is computed from the original background wind field, the true vector observations, and the "radar vector observations" as described in Section 2.

At a point with two Doppler wind estimates, the measured radial component from TDWR will equal the radial component of the "radar vector observation". The difference between the radial component measured by NEXRAD and the corresponding radial component of the "radar vector observation" dependents on the angle between the two radar beams. When the angle is 90°, the difference is zero. As the angle decreases to 0°, the difference increases to the difference between the the TDWR and NEXRAD measurements, and at 0°, a "radar vector observation" is equal to the single Doppler "radar vector observation" computed from only the TDWR data. The TDWR data were chosen to follow the NEXRAD data in the MSDA process since the TDWR is located closer to the Orlando International Airport.

5. DISCUSSION OF MSDA AND DDA

In traditional dual Doppler analysis (DDA), a wind vector is computed at each analysis point with two Doppler observations. The resulting wind vector exactly agrees with both Doppler values. When the two radars have independent looks at the wind field, defined as 30° or more between the directions of the beams, DDA generates very accurate estimates of the wind. This points to two difficulties that arise with DDA in an analysis system which must produce an analysis at each grid point. First, not every grid point will have a Doppler return from each radar. Second, when the two radars do not have independent looks at the wind field, DDA becomes numerically unstable. This baseline instability gets progressively worse as the angle between the radar beams decreases. The first difficulty can be overcome, but will result in an increase in complexity relative to MSDA.

MSDA on the other hand, automatically handles incomplete Doppler data, and does not have a baseline instability. When two Doppler values are available at points where the two radar looks are independent, the "radar vector observation" is very close to the wind estimate produced by DDA. When the two radars do not have independent looks, MSDA produces a numerically stable "radar vector observation" with one high quality component, a Doppler measurement. The other component is derived from the non–Doppler data sources. At points with only one Doppler value, MSDA again produces a "radar vector observation" with one high quality component. Structural constraints imposed during the implied filtering in the final analysis step ensure that the wind structure in each of the sub–areas blends well.

Our implementation of MSDA was developed as a rapid prototype for this demonstration. As such, it has many desirable properties. However, it also has some weaknesses that we will address in the future. In regions with favorable geometry and returns from both radars, the "radar vector observations" are in close agreement with DDA, but are then smoothed by the analysis. When the two radars are looking in nearly the same direction, the NEXRAD data are largely overwritten by the TDWR data. This is true, for example, even when the analysis point is closer to the NEXRAD than the TDWR. This weakness could be alleviated with a weighting between the two radars to take into account the geometry of the analysis region. Each "radar vector observation" has a different level of quality due to whether the observation was built from one or two Doppler estimates, and the radar geometry at the observation location. This is not currently taken into account. Lastly, our implementation of MSDA can be used with any number of Doppler radars, but even with 3 or more Doppler radars it will have the weaknesses cited above.

Our MSDA implementation is equivalent to producing "radar vector observations" using weighted least squares with the following assumptions: the weights are inversely proportional to the error variance of the data, the TDWR error variance is infinitely small relative to the NEXRAD error variance, and the NEXRAD error variance is infinitely small relative to the error variance of the background wind field. This suggests optimization as a path to improving the MSDA technique. In addition, improvements are underway to generate a background wind field containing pre–derived dual Doppler wind vectors. This allows the existing analysis scheme to improve analyses in dual Doppler regions, by reducing the error in the background wind, and in single Doppler regions by increasing the accuracy of the tangential components of the "radar vector observations".

6. TWO EXAMPLES

The T–LAPS analysis region was 120 km x 120 km in the horizontal, centered on the Orlando International Airport,

and extended from the surface to a height of 500 mb. The grid resolution was 2 km x 2 km x 50 mb, and the analysis was performed every 5 minutes.

This fine grid resolution and rapid update rate were achieved by using a "cascade of scales". First, the winds were analyzed to a 10 km x 10 km x 50 mb grid, every 30 minutes. All of the available data sources were used in this analysis, and the background wind field was derived from the Mesoscale Analysis and Prediction System (MAPS) (Benjamin *et al.*, 1991). Next, the final analysis was performed every 5 minutes, using only the Doppler data and automated ground station data, LLWAS and ASOS/AWOS, with the latest 10 km analysis providing the background wind field.

The figures show the analyzed winds at 400 ft AGL, and the NEXRAD reflectivity resampled to the 2 km grid. The winds are displayed on a 4 km grid to reduce visual clutter, and a 5 m/s wind arrow is shown for scale in the upper right corner of each figure. The airport runways are shown in the center. The four outlines are lakes, and the coast appears along the northeast in each figure. Both examples are from August 20, 1992.

Figure 1 shows the wind and reflectivity at 21:30 GMT. A gust front, shown by both a reflectivity thin line and a line of convergence in the wind field, is being produced by a storm off the coast to the southeast of the analysis region. Later in the day, this gust front collides with a line of decaying storms northwest of the airport, spawning a new convective storm system. Figure 2 shows the wind and reflectivity at 23:55 GMT associated with the new convective storm.

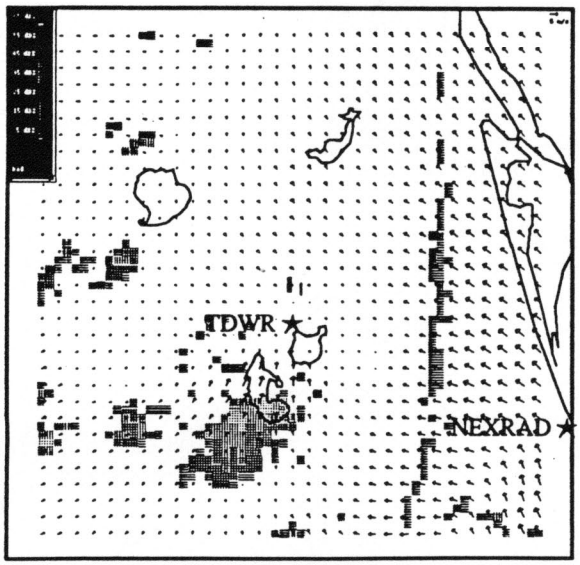

Figure 1. Wind and Reflectivity
(Aug. 20, 1992 21:30 GMT)

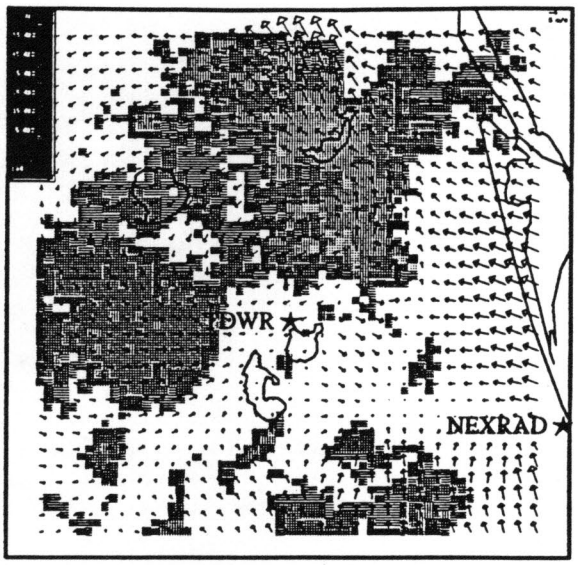

Figure 2. Wind and Reflectivity
(Aug. 20, 1992 23:55 GMT)

7. ACKNOWLEDGEMENTS

We would like to thank the Melbourne National Weather Service Office for access to the NEXRAD base data, and Thomas Schlatter and Stanley Benjamin at NOAA/ERL/FSL for providing wind data from the Mesoscale Analysis and Prediction System for the background wind for T–LAPS. We would like to thank Russ Bolton and Jerry Starr at Computer Science–Raytheon for modifying their data base to provide the ground station data in our analysis region. Finally, we would like to thank the LLWAS program office for expediting the installation of the LLWAS 3 anemometer network at the Orlando International Airport.

REFERENCES:

Albers, S.C., 1992: The laps wind analysis. *Fourth Workshop on operational meteorology*, Whistler, B.C., Canada.

Barnes, S., 1964: A technique for maximizing details in numerical weather map analysis. *J. Appl. Met.*, 3, no 4.

Benjamin, S. G., *et al.*, 1991: An isentropic three–hourly data assimilation system using ACARS aircraft observations. *Monthly Weather Review*, vol. 119, no 4.

McGinley, J., S. Albers, P. Stamus, 1991: Validation of a composite convective index as defined by a real–time local analysis system. *Wea. Forecast.*, 6, 337–356.

Adjoint-Method Retrievals of Microburst Winds From TDWR Data*

Qin Xu, Chong-Jian Qiu, Jin-Xiang Yu, Hong-Dao Gu
CIMMS/CAPS, University of Oklahoma

Marilyn Wolfson
Lincoln Laboratory, MIT

1. Introduction

The simple adjoint (SA) method of Qiu and Xu (1992, henceforth referred to as QX92) was recently upgraded and tested with the Phoenix-II data for retrieving the low-altitude winds from single-Doppler scans (Xu et al. 1993a,b, henceforth referred to as XQY93a,b). The major results can be briefly reviewed as follows: (i) Using multiple time-level data with the adjoint formulation makes the retrieval more accurate and less sensitive to the observational error. (ii) Imposing a weak nondivergence constraint can suppress the spurious divergence caused by the data noise and improve the retrieval. (iii) Retrieving the eddy coefficients improves the wind retrieval. (iv) Retrieving the time-mean residual term improves the wind retrieval.

Although the results in XQY93a,b were encouraging, the Phoenix-II data used in XQY93a,b were collected on non-storm days with chaff dispensed from an aircraft. The real challenge is to test the SA method with storm data. A microburst case is selected for the test in this paper.

2. 11 July 1988 Microburst case

On 11 July, a very strong microburst (> 35 m/s differential velocity) occurred at the Denver Airport during the 1988 TDWR (Terminal Doppler Weather Radar) operational test and evaluation (Elmore et al. 1990, Proctor and Bowles 1992). Dual Doppler coverage was provided by the TDWR testbed radar (FL2, operated by MIT Lincoln Laboratory) and the UND (University of North Dakota) radar (see Fig. 1). The operational scan strategy executed by FL2 included a surface sector scan over the airport every minute. This surface scan was matched nearly simultaneously (avg. within 3.5 sec) by UND. The polar data from each radar were thresholded at 5 dB SNR and median smoothed with a 5 gate x 3 degree filter (at least 8 good values out of 15 required). The data were then sampled to a 250 m resolution Cartesian grid (at the level of z = 190 m above the FL2 radar site).

Surface anemometer data from the 12 station Low Level Wind Shear Alert System (LLWAS) were also collected during the experiment (see Fig. 1). Several of the stations in 1988 suffered from wind sheltering problems (Liepins et al. 1990) that have since been remedied by raising the sensor height.

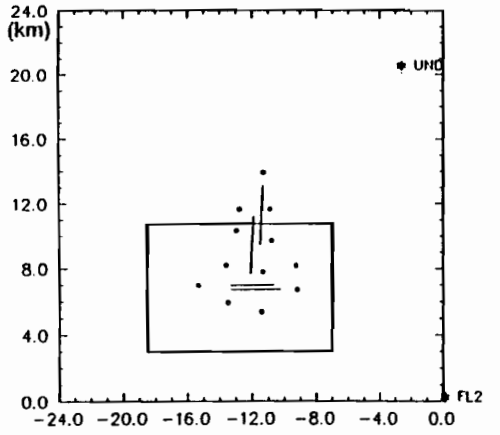

Fig. 1. Locations of airport runways, radars and LLWAS stations. The inner rectangular domain indicates the region where the winds are retrieved in Fig. 2a.

3. Method description

As in XQY93b, the radial-component wind v_r is used as a "tracer" field and is governed by the following approximate radial-component momentum equation:

$$\partial_t v_r + \mathbf{v}_m \cdot \nabla v_r - v_{\alpha m}^2/r - \kappa \nabla_H^2 v_r = F_m, \quad (1)$$

where v_α is the cross-beam wind, $\mathbf{v}$ the horizontal vector wind, $(\cdot)_m \equiv (1/\tau)\int_0^\tau (\cdot)dt$ the time-mean operator, F the unknown residual forcing (mainly the pressure gradient and vertical advection). The boundary and initial values are given by the observed v_r.

The objective is to find the best estimate of ($\mathbf{v}_m$, κ, F_m) in (1) that gives the best "prediction" of the radial wind v_r in terms of minimizing the following cost-function

$$J \equiv \{\{P_1\Delta^2 + P_2\Delta_m^2 + P_3 d_m^2 + P_4 \zeta_m^2\}\}_m. \quad (2)$$

Here $\{\{(\cdot)\}\} \equiv (1/\Omega)\int\int(\cdot)d\Omega$ is the area-mean operator over the retrieval domain Ω; P_1 and P_2 are nondimensional weights, $\Delta \equiv v_r - v_{rob}$, $\Delta_m \equiv v_{rm} - v_{robm}$, and $(\cdot)_{ob}$ the observed value of $(\cdot)$; P_3 and P_4 are dimensional weights (in unit m^2), $d_m \equiv \nabla_H \cdot \mathbf{v}_m$ the divergence, and $\zeta_m \equiv \mathbf{k} \cdot \nabla_H \times \mathbf{v}_m$ the vorticity. The minimum of J can be approached by numerical iteration along the gradient of J with respect to ($\mathbf{v}_m$, κ, F_m). The gradient is computed at each step of iteration by a explicit expression derived from the adjoint formulation similar to (2.7) of XQY93b.

The optimal retrieving time period τ should cover 4 sequential scans, i.e., $\tau = 3\Delta\tau$. The weights are given by

$$\begin{aligned} P_1 &= [\tau/(t+\Delta t)]^{1/2}, \\ P_2 &= 0.02 P_{1m} \text{ with } P_{1m} \equiv (P_1)_m, \\ P_3 &= k_3 \sigma_{vr}^2 P_{1m} \text{ with } k_3 = 30 \sim 200\ m^2, \\ P_4 &= k_4 \sigma_{vr}^2 P_{1m} \text{ with } k_4 = 100 \sim 600 m^2, \end{aligned} \quad (3)$$

where σ_{vr} is the root mean square amplitude of v_r. The choice of the time-dependent form for P_1 was explained in QX92. With the above specified value for P_2, the weak form of the constraint $\Delta_m = 0$ can reduce the error in the estimated cross-beam wind. The relative strength of the weak divergence (or vorticity) constraint is controlled by k_3 (or k_4). As long as k_3 (or k_4) is in the optimal range shown in (3), the retrieval is not very sensitive to k_3 (or k_4). The weights in (3) are consistent with those in XQY93a,b, but k_4 and the last term in (2) are new here.

4. Results

The SA method is tested with the microburst data for a continuous period (22:04-22:33). The averaged (over 25 time-levels) RMS errors and correlation coefficients between the retrieved and observed variables are listed

*A portion of this work was sponsored by the Federal Aviation Administration. The views expressed are those of the authors and do not reflect the official policy or position of the U.S. Government.

in Table 1. When the observed radial winds are used in the final results, the vector RMS errors for $\mathbf{v}_m$ reduce to those for $v_{\alpha m}$ in Table 1. The retrieved wind field is compared with the observed in Fig.2a-b. The correlation diagram is shown in Fig. 3, where the RMS error and correlation coefficient between the retrieved and observed wind components are also listed. The retrievals from FL2 radar data are better than those from UND radar data.

The accuracy of the retrievals are affected mainly by three factors: the data noise, the temporal fluctuation of the residual forcing (i.e., the equation error), and the wind direction relative to the radar beam.

Using the wind field retrieved at the previous time level as an initial guess can reduce the CPU cost, but may not always improve the accuracy. Extrapolating the LLWAS data to the grid level of z = 190 m and using it as a weak constraint may (or may not) improve the retrieval, if the surface winds are well (not well) correlated to the Doppler radial winds at the the grid level.

Table 1. Statistics of the retrievals (with FL2 radar)

	$\mathbf{v}_m$ m/s	$v_{\alpha m}$ m/s	d_m $10^{-3}s^{-1}$	ζ_m $10^{-3}s^{-1}$	F_m $10^{-2}m/s^2$
FL2 radar:					
RMS error	3.30	2.99	4.75	3.16	1.25
Correlation	0.92	0.83	0.60	0.22	0.77
UND radar:					
RMS error	4.53	4.37	5.34	3.32	1.41
Correlation	0.84	0.65	0.48	0.17	0.68

5. Conclusion

In addition to the earlier findings reviewed in section 1, it is found in this paper that using the weak vorticity constraint also improves the retrieval, especially for microburst cases. Using the previous time-level retrieval as an initial guess can reduce the CPU cost. Optimal uses of the surface wind data need further investigations.

Acknowledgment

This work is supported by the NOAA contract NA90-RAH00078 and NSF Grants ATM-9113906 at CIMMS and ATM-8809862 at CAPS, University of Oklahoma.

References

Elmore,K.L., M.K. Politovich, and W.R. Sand, 1990: The 11 July 1988 Microburst at Stapleton International Airport, Denver, CO. Preprints, 16th Conf. on Severe Local Storms, Kananaskis Park, Amer. Meteor. Soc.,368-372.

Liepins, M.C., M.M. Wolfson, D.A. Clark, and B.E. Forman, 1990: A comparison of anemometer and Doppler radar winds during wind shear events. Preprints, 16th Conf. on Severe Local Storms, Kananaskis Park, Amer. Meteor. Soc., 356-361.

Proctor, F.H. and R.L. Bowles, 1992: Three-dimensional simulation of the Denver 11 July 1988 microburst-producing storm. Meteorol. Atmos. Phys., 49, 107-124.

Qiu, C. J. and Q. Xu, 1992: A simple adjoint method of wind analysis for single-Doppler data. *J. Atmos. & Oceanic Technology*, **9**, 588-598.

Xu, Q., C. J. Qiu, and J. X. Yu, 1993a: Adjoint-method retrievals of low-altitude wind fields from single-Doppler reflectivity measured during Phoenix II. (Conditionally accepted) *J. Atmos. & Oceanic Technology*.

Xu, Q., C. J. Qiu, J. X. Yu, 1993b: Adjoint-method retrievals of low-altitude wind fields from single-Doppler wind data. (Conditionally accepted) *J. Atmos. & Oceanic Technology*.

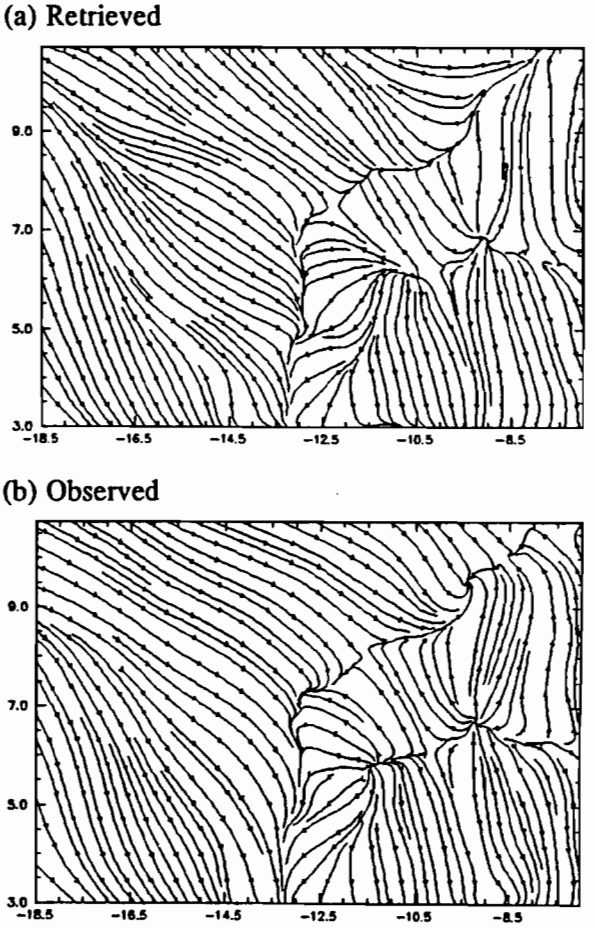

Fig. 2. Comparison between the (a) retrieved (from FL2 data) and (b) dual-Doppler observed time-mean wind fields at z = 190 m for 22:10-14, 16, July 11, 1988.

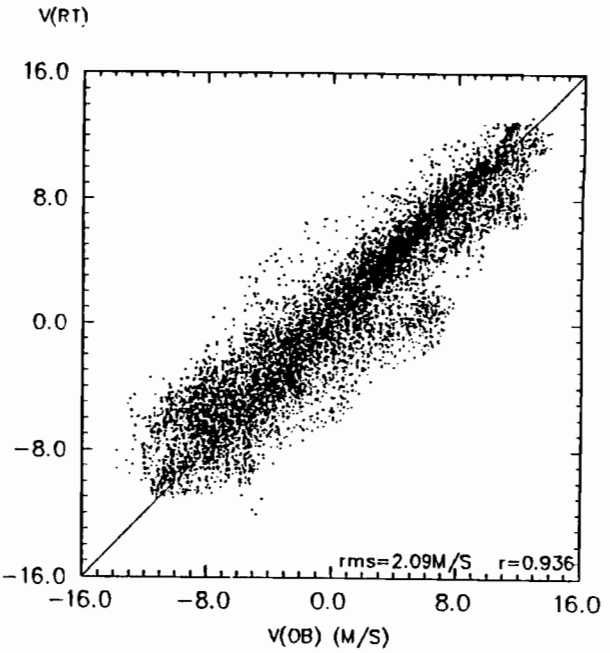

Fig. 3. Correlation diagram between the retrieved and dual-Doppler observed winds (for every 5th time-level during the period of 22:04-33).